Acta Pharmaceutica Sinica B 2025;15(11):5908−5932

Chinese Pharmaceutical Association
Institute of Materia Medica, Chinese Academy of Medical Sciences

Acta Pharmaceutica Sinica B

www.elsevier.com/locate/apsb
www.sciencedirect.com

ORIGINAL ARTICLE

DNAzyme targeting RIP3 suppresses NLRP3-mediated necroinflammation for the treatment of inflammatory diseases

Jiaxin Jia[a], Hugang Zhang[a], Guangxu Fang[a], Yang Li[a], Kai Wen[a], Hanyu Liu[a], Haobo Han[a,*], Quanshun Li[a,b,*]

[a]*Key Laboratory for Molecular Enzymology and Engineering of Ministry of Education, School of Life Sciences, Jilin University, Changchun 130012, China*
[b]*China-Singapore Belt and Road Joint Laboratory on Liver Disease Research, The First Hospital of Jilin University, Changchun 130012, China*

Received 24 February 2025; received in revised form 19 May 2025; accepted 12 June 2025

KEY WORDS

DNAzyme;
Necroinflammation;
Receptor-interacting protein kinase 3;
Gene therapy;
Inflammatory diseases;
Polyamidoamine;
NOD-like receptor family pyrin domain-containing 3;
MCC950

Abstract Necroptosis, a form of programmed cell death, initiates a series of biological responses and further culminates in necroinflammatory processes, consequently limiting the efficacy of cytokine antagonists in treating inflammatory diseases. To address this issue, DNAzyme R3-Dz specifically targeting receptor-interacting protein kinase 3 (RIP3) mRNA, a necrosome component, has been successfully developed and studied to elucidate the mechanism in cleaving its target mRNA. Then a polyamidoamine (PAMAM) derivative was constructed through the modification of nucleobase analog (termed AP) to achieve the R3-Dz delivery to macrophages. The AP/R3-Dz nanoparticles effectively downregulated the RIP3 expression, leading to subsequent decrease in the levels of reactive oxygen species (ROS) and damage-associated molecular patterns (DAMPs), ultimately inhibiting the necroinflammatory processes mediated by the NOD-like receptor family pyrin domain-containing 3 (NLRP3). Finally, AP/R3-Dz nanoparticles and their combination with the NLRP3 inhibitor MCC950 suppressed the necrotic phenotype and ameliorated the disease progression in diverse models, including gouty arthritis, autoimmune hepatitis and rheumatoid arthritis. In summary, the AP/R3-Dz nanoparticles in combination with MCC950 have been demonstrated to achieve the intervention in necroptosis and inflammation by dual disruption of the intricate feedback loop of necroinflammation and thus have promising potential in the treatment of inflammatory diseases.

*Corresponding authors.
E-mail addresses: quanshun@jlu.edu.cn (Quanshun Li), hanhaobo@jlu.edu.cn (Haobo Han).

Peer review under the responsibility of Chinese Pharmaceutical Association and Institute of Materia Medica, Chinese Academy of Medical Sciences.

https://doi.org/10.1016/j.apsb.2025.09.002

1. Introduction

Acute inflammation represents a localized defensive response, primarily elicited by microbial infection or tissue destruction[1]. Once the immediate threat is addressed, resolving this inflammation becomes crucial for homeostasis restoration[2]. However, if natural immune system fails to adequately eliminate inflammatory stimuli, it can promote persistent immune responses and ongoing tissue damage by mononuclear macrophages and lymphocytes, consequently driving the development of chronic inflammatory diseases such as systemic lupus erythematosus (SLE), chronic tophaceous gout and rheumatoid arthritis (RA)[3,4]. To date, although the pathogenesis of these inflammatory diseases has been extensively investigated, the understanding and clinical interventions largely focus on the regulation of pro-inflammatory cytokine network[5]. For instance, several biologics, such as anakinra, tocilizumab and infliximab, have shown therapeutic efficacy in ameliorating the symptoms of inflammatory diseases by specifically targeting and disrupting the pathway of cytokines[6,7]. Unfortunately, despite the achievements of these biologics, significant hurdles are yet to be overcome. Typically, these biologics offer palliative effect, meaning that they primarily suppress the symptoms rather than address the underlying cause to achieve a cure[8]. Moreover, over half of patients treated with these biologics could not obtain anticipated therapeutic outcomes and a subset of patients developed new inflammatory diseases[9]. Not surprisingly, blocking downstream inflammatory effectors often results in a delayed and insufficient treatment, since this strategy fails to resolve the primary contributor of inflammation, thereby limiting the therapeutic efficacy. Thus, it is crucial to investigate and trace the roots back to the factors that drive and exacerbate the inflammatory response, in order to effectively mitigate the progression of inflammatory diseases.

Necroptosis, a form of programmed cell death, plays a pivotal role in triggering the inflammatory response, commonly referred as necroinflammation[10]. This process involves the phosphorylation of receptor-interacting protein kinase (RIP) 1 and RIP3, and recruits the mixed lineage kinase-like protein (MLKL) polymerization on the plasma membrane, ultimately culminating in the generation of reactive oxygen species (ROS) and plasma membrane rupture[11]. Consequently, necroptosis leads to the release of intracellular contents, specifically damage-associated molecular patterns (DAMPs), which further activates the formation of NOD-like receptor family pyrin domain-containing 3 (NLRP3) inflammasome to trigger a cascade of inflammatory events[12]. Moreover, the excessive pro-inflammatory cytokines, in turn, prime innate immune cells, amplifying the inflammatory response and ROS production[13]. The increased ROS then stimulates the RIP1 phosphorylation and recruits RIP3 to form the necrosome, executing the necroptosis program[14]. Indeed, RIP1 inhibitors or RIP3 deficiency have been demonstrated to not only alleviate the tissue necrosis but also ameliorate the inflammatory diseases, suggesting that the blockade of necroptosis plays a crucial role in suppressing the inflammation[15]. Thus, the timely termination of necroinflammation is crucial to prevent the progression of inflammatory cascade and subsequently promote the tissue repair.

Deoxyribozyme (DNAzyme) is a kind of catalytically functional DNA fragment that has emerged to be a powerful tool in gene therapy[16]. Owing to its programmability and potent catalytic efficiency, DNAzyme can be precisely engineered to target specific pathogenic mRNA sequences and catalyze the cleavage of phosphodiester bonds, thereby facilitating the gene silencing[17]. Two prototypical examples, "SB010" and "Dz13" targeting human *GATA*-3 mRNA and *c-Jun* mRNA, have been utilized in clinical trials for inflammatory and cancer diseases, respectively[18,19]. In contrast to other gene silencing approaches, DNAzyme offers significant advantages including high stability, low immunogenicity and the capacity to catalyze reactions autonomously under physiological conditions without requiring accessory proteins[20]. However, similar to other nucleic acids, DNAzyme molecules face challenges in systemic administration, as they are vulnerable to the nucleases' degradation and the rapid metabolism by reticuloendothelial system[21]. To tackle these challenges and expand potential applications, we have developed polyamidoamine (PAMAM) derivatives for the delivery of oligonucleotides in treating RA, which exhibited an ability to target affected tissues and obtain favorable therapeutic efficacy[22]. PAMAM dendrimers, characterized as three-dimensional soft nanoparticles with NH_2 terminal groups, offer the advantage of versatile surface modifiability to meet specific needs[23]. Moreover, the low immunogenicity and potential *per se* anti-inflammatory properties have highlighted their potential as a promising option for the disease treatment, particularly in the personalized medicine[24]. Inspired by natural DNA architectures, a nucleobase-modified strategy has been employed to construct PAMAM derivatives, mimicking DNA's supramolecular assembly[25,26]. This approach could improve the transfection efficiency and reduce cytotoxicity through optimized hydrogen bonding interactions, similar to DNA hybridization. By incorporating reversible and non-covalent binding dynamics, these modified PAMAM dendrimers provide an adaptable system that can respond to environmental stimuli for the targeted delivery of nucleic acids[27].

In this study, the DNAzyme R3-Dz specifically targeting *RIP3* mRNA was successfully screened, and its molecular mechanism in cleaving the target mRNA was further elucidated. To enhance its delivery to macrophages, a PAMAM derivative (termed AP) was constructed through the modification of 2-amino-6-chloropurine. The AP/R3-Dz nanoparticles exhibited an inhibition of necroinflammation by specifically targeting and silencing *RIP3* mRNA in macrophages, thereby disrupting key necroptotic pathways and attenuating the NLRP3 inflammasome-mediated inflammatory cascade. To evaluate the *in vivo* therapeutic efficacy of the combination of AP/R3-Dz nanoparticles with the NLRP3 inhibitor MCC950, gouty arthritis (GA), autoimmune hepatitis (AIH) and RA models were constructed which enabled us to thoroughly assess their impact on different aspects of inflammation and tissue damage. Moreover, our investigations delved into the mechanism by which AP/R3-Dz nanoparticles and MCC950 exerted their effects, particularly focusing on the role in silencing RIP3,

inhibiting necroptosis and attenuating the activation of NLRP3 inflammasome. Taken together, our studies elucidated the comprehensive anti-inflammatory and tissue-protective mechanism of R3-Dz and MCC950, thereby substantiating their potential as a versatile and effective therapeutic agent for various inflammatory diseases (Scheme 1).

2. Materials and methods

2.1. Materials

Amine-terminated polyamidoamine (PAMAM) dendrimer with the generation of 5.0 (ethylenediamine core) (121, lot 0221-03-E5.0-LD-W) was purchased from Dendritech (Midland, MI). Polyethylenimine (PEI, 408727), 2-amino-6-chloropurine (A114035), $MgCl_2$ (M8266) and lipopolysaccharides (LPS, L2880) were provided by Sigma−Aldrich (St Louis, MO, USA). Z-Val-Ala-Asp (OMe)-FMK (Z-VAD) (MB3313) and MCC950 sodium (MB3021) were purchased from Meilunbio (Dalian, China). The siRIP1 (5′-GGAGCAAACUGACUAAGGATT-3′), siRIP3 (5′-CGACGAUGUCUUCUGUCAATT-3′), the negative control siRNA (NC) (5′-UUCUCCGAACGUGUCACGUTT-3′) and FRET-substrate were synthesized by GenePharma (Suzhou, China). The DNAzyme (Dz), inactive DNAzyme (iDz), fluorescence-labelled DNAzymes and primers were provided by Sango Biotech (Shanghai, China), and their sequences were listed in Supporting Information Tables S1 and S2. Dulbecco's modified Eagle's medium (DMEM), fetal bovine serum (FBS), 1% penicillin/streptomycin and phosphate buffered solution (PBS, pH7.4) were acquired from Gibco (Grand Island, NY, USA). 1 mol/L $MgCl_2$ (ST269) was purchased from Beyotime (Nanjing, China). 1 mol/L Tris−HCl (pH7.5, T1140) was provided by Solarbio (Beijing, China). TRNzol Universal reagent (DP424) for RNA isolation was obtained from Tiangen Biotech (Beijing, China). Hoechst (R37605), DNase (EN0521), 4,6-diamidino-2-phenylindole (DAPI) (62248) and LysoTracker Red (L12492) were purchased from Invitrogen (Carlsbad, CA, USA). DCF-DA (MX4802) and Mito-SOX red mitochondrial superoxide indicator (MX4313) were purchased from MaoKang Biotechnology (Shanghai, China). Dihydroethidium (DHE, D0079) was acquired from MCE (Monmouth Junction, NJ, USA). The reagents used in the construction of animal models were listed as follows: concanavalin A (Con A) and uric acid (U0881), Sigma−Aldrich (St. Louis, MO, USA); complete Freund's adjuvant (CFA) (7009), incomplete Freund's adjuvant (IFA) (7002) and type II bovine

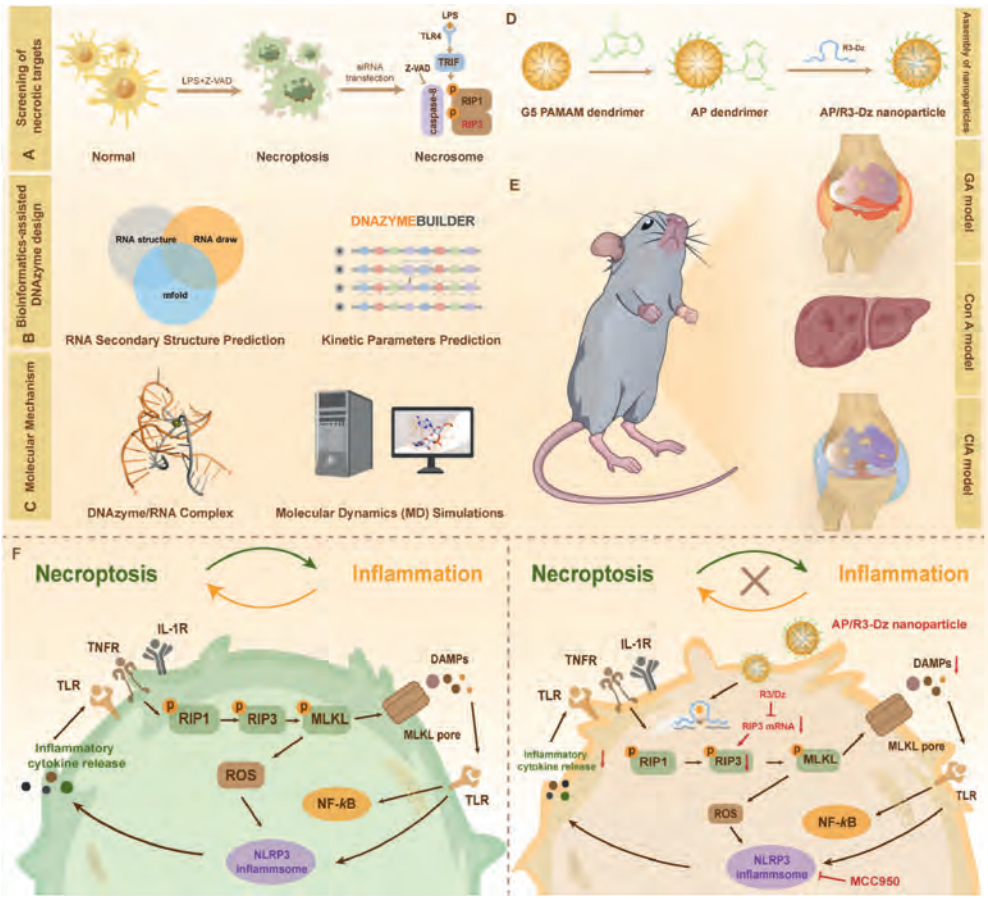

Scheme 1 AP/DNAzyme and MCC950 dual suppresses the NLRP3-mediated necroinflammation for the treatment of inflammatory diseases. (A) Establishment of necroptosis model to screen the necrotic targets in macrophages. (B) Bioinformatics-assisted DNAzyme design, including the prediction of RNA secondary structure and kinetic parameters. (C) Molecular dynamics (MD) simulation of DNAzyme/RNA complex. (D) Construction of AP derivative and AP/R3-Dz nanoparticles. (E) The *in vivo* therapeutic efficacy of AP/R3-Dz nanoparticles in GA, AIH and RA models. (F) Dual intervention through the combination of AP/R3-Dz and MCC950 to block the RIP3−NLRP3-mediated necroinflammatory loop.

(20022), Chondrex (Woodinville, WA). The relevant kits were used in the present studies: CellTiter-Glo® Luminescent Cell Viability Assay kit, Promega (Madison, WI, USA); Duolink® *In-Situ* Red Starter kit, Mouse/Rabbit (DUO92101), Sigma−Aldrich (St. Louis, MO, USA); IL6 Mouse ELISA kit (BMS603-2), IL1β Mouse ELISA kit (BMS6002) and TNF Mouse ELISA kit (BMS607-3), Invitrogen (Carlsbad, CA, USA); IL18 Mouse ELISA kit (MM-0169M2) and HMGB1 Mouse ELISA kit (MM-44107M1), Meimian Industrial Co., Ltd. (Jiangsu, China); PrimeScript RT reagent kit (RR037A) and TB Green Premix Ex Taq kit (Tli RNaseH Plus, RR820A), TaKaRa (Dalian, China); BCA protein assay kit (BB3401), Bestbio (Shanghai, China); DCF-DA Cellular Reactive Oxygen Species Detection kit (S0033S), Beyotime (Nanjing, China); Fluorescent Multiplex Reagent kit (RC0086-34RM), Recordbio (Shanghai, China); Safranin-O/Fast Green kit (G1053), Toluidine blue dye solution (G1032) and H&E Staining kit (G1003), Servicebio (Wuhan, China).

2.2. Synthesis and characterization of AP

The AP synthesis process was referred to our previous report[25,26]. In brief, 50.0 mg PAMAM and 28.5 mg 2-amino-6-chloropurine were dissolved in 10 mL of ethanol/water solution (50%, *v/v*), and 17.0 mg sodium bicarbonate was added to neutralize the acid during the reaction. The solution was stirred at 80 °C for 24 h, dialyzed in distilled water for 48 h (molecular weight cut-off: 3500 Da) and lyophilized to obtain the product AP. The structure of AP derivative was characterized by AVANCE DMX 500 NMR spectrometer (Bruker, Rheinstetten, Germany) using the MestReNova 10.0.2 software. The morphology of AP/R3-Dz nanoparticles (N/P ratio of 10.0) was observed by Hitachi H800 transmission electron microscope at an accelerating voltage of 200 kV. The hydrodynamic diameter and zeta potential of nanoparticles at different N/P ratios were measured by Zetasizer Nano ZS90 (Malvern, UK) using the Malvern Zetasizer 7.11 software.

2.3. Design and screening of DNAzyme targeting RIP3

The prediction platforms for RNA secondary structure including RNAdraw (version 1.1), RNA Structure (version 6.1) and Mfold (http://www.unafold.org/) were used to retrieve conserved AU/GU motif of *RIP3* mRNA (NM_019955.2) to guide the design of DNAzyme libraries. The Venn diagram illustrated the overlap between target sequences screened from multiple databases. The binding arm of DNAzyme (9 nt) was designed to be complementary to the sequence flanking the cleavage site in the predicted structural region. The software DNAzymeBuilder (https://iimcb.genesilico.pl/DNAzymeBuilder) was utilized to predict the k_{obs} values of DNAzymes. The sequences of all the assessed DNAzymes were shown in Supporting Information Table S1.

2.4. In vitro cleavage assay

Multiple-turnover kinetic cleavage reactions were performed in 50 mmol/L Tris buffer (pH 7.5), containing 150 mmol/L NaCl, 2 mmol/L $MgCl_2$, 4 μmol/L substrate and 2 μmol/L DNAzyme at 37 °C. DNAzyme and substrates were annealed in 50 mmol/L Tris buffer (pH 7.5) by heating at 95 °C for 4 min and cooling down to room temperature. Reactions were initiated by adding 150 mmol/L NaCl and 2 mmol/L $MgCl_2$ and terminated by the addition of EDTA to 10 mmol/L, followed by the PAGE analysis. Gel images were visualized using Universal Hood II system (Bio-Rad, USA). The k_{obs} values were calculated by fitting the percentage of substrates cleaved and the reaction time (min) under pseudo-first-order kinetic conditions. The equation was listed as the following Eq. (1):

$$Y = \mathrm{a}\,(1\text{-}\exp(\text{-}k_{\mathrm{obs}}\,t)) \quad (1)$$

where Y is the percentage of substrates cleaved at time (t).

The fluorescence resonance energy transfer (FRET) substrate was used for multiple turnover kinetic cleavage reactions. The cleavage reactions were performed as described above. Samples were excited at 494 nm, and the spectra were monitored from 510 to 600 nm using Shimadzu RF-6000 fluorescence spectrophotometer (Kyoto, Japan).

2.5. Molecular dynamics (MD) simulation

The structure of DNAzyme/substrate complex was referenced from PDB entry 7PDU[28]. Accordingly, the post-catalytic structure (R3-Dz/Product, R3-Dz/P) and pre-catalytic structure (R3-Dz/Substrate, R3-Dz/S) were constructed by base editing using Discovery studio 2019 (Accelrys, San Diego, USA). In addition, the dG_{14} site in R3-Dz/S was mutated to C_{14} to construct the R3/Dz^{G14C}/S varient. Three Mg^{2+} ions were added to the simulated system as previously described[28]. To explore the molecular dynamics of DNAzyme/substrate complex systems, GaMD was used with OL15 force fields of DNA, OL 3 force fields of RNA and the TIP3P water model. The simulations were carried out in a cube box (15 Å) with periodic boundary conditions under constant temperature (310 K) and 1 atm constant pressure with a time step of 2 fs. To analyze the conformational changes and the backbone stability of complex systems during simulation, root-mean-square deviation (RMSD) and root-mean-square fluctuation (RMSF) were analyzed using the Cpptraj module in Amber 20. MM/PBSA was calculated by the MMPBSA. py program in the Amber 20 package using Poisson Boltzmann (PB) implicit solvent models. The VMD 1.9.3 software was used to visualize the MD trajectories. All structural figures were prepared using PyMOL 2.5.7 Molecular Graphics System.

2.6. Induction of necropotosis in macrophages

The RAW264.7 cells were seeded in 6-well plates (6.0×10^5 cells/well) or 96-well plates (6.0×10^3 cells/well), and stimulated with 0.1 μg/mL LPS and 25 μmol/L Z-VAD for 24 h. For transmission electron microscopy analysis, the cells were fixed with 2.5% glutaraldehyde in 0.1 mol/L cacodylate buffer (pH 7.4), followed by 1% osmium tetroxide for 1 h. Samples were then rinsed in PBS, dehydrated in a graded ethanol, incubated in 100% acetone and ultimately embedded in paraffin. Ultrathin sections were performed, mounted on copper grids, and finally stained with uranyl acetate and lead citrate at room temperature. The prepared samples were examined and photographed using HT7700 transmission electron microscope (Hitachi, Tokyo, Japan). For cell death analysis, the cells were stained with 2 μg/mL PI and 5 μg/mL Hoechst reagent in PBS for 30 min. After washing with PBS three times, the cells were analyzed on IX73P1F fluorescence microscope (Olympus, Tokyo, Japan). The above cells were further examined by CytoFLEX flow cytometry (Beckman Coulter, Brea, CA, USA) and all relevant data were analyzed using FlowJo *software* (version 10.0). For cell viability analysis, the cells were treated with CellTiter-Glo® Luminescent

Cell Viability kit and performed according to the manufacturer's instructions. Briefly, the supernatants were removed after the cell culture, and 100 μL fresh DMEM and 100 μL CellTiter-Glo® reagent were added into the well. After shaking for 2 min, the cells were incubated at room temperature for 10 min and the luminescence signals were monitored using Infinite200 Pro microplate reader (Tecan, Mannedorf, Switzerland). The data from the control group were set as 100%, and the survival of cells in other wells was normalized relative to this reference.

2.7. R3-Dz transfection

The cells were inoculated into 6-well plates (6.0×10^5 cells/well), and transfected with siRIP3 (150 nmol/L), R3-Dz (3 μg/mL) and R3-iDz (3 μg/mL) using AP as the carrier (N/P ratio of 10.0) in FBS-free DMEM for 6 h. Afterward, the medium was replaced by 10% FBS-containing DMEM, and the cells were cultured for 42 h. For the necroptosis assay, transfections were conducted as described above, and the cells were further cultured for 18 h and stimulated with 0.1 μg/mL LPS and 25 μmol/L Z-VAD for additional 24 h.

2.8. Intracellular ROS level assay

The cells were cultured in 6-well plates at 37 °C overnight (initial density of 6.0×10^5 cells/well). After the transfection with nanoparticles and the induction of necroptosis as above, the cells were washed with PBS three times and incubated with DCF-DA (10 μmol/L) or Mito-SOX (500 nmol/L) for 30 min. Finally, the cells stained with DCF-DA (10 μmol/L) were subjected to analysis using Olympus IX73P1F fluorescence microscope (Tokyo, Japan) and CytoFLEX flow cytometry (Beckman Coulter, Brea, CA, USA). The cells stained with Mito-SOX (500 nmol/L) were subjected to the detection using Spectramax iD3 multi-mode microplate reader (Molecular Devices, Sunnyvale, CA, USA) with an excitation wavelength at 510 nm and an emission wavelength at 580 nm, respectively.

2.9. Measurement of cytokines and HMGB1 in the cell supernatant

The cell supernatant was collected, centrifuged at $500 \times g$ for 10 min to discard the precipitates and then utilized to determine the concentration of IL6, IL18, TNF, IL1β and HMGB1 by the respective ELISA kits. The absorbance was measured at 450 nm using Tecan Infinite200 Pro microplate reader (Tecan, Mannedorf, Switzerland).

2.10. Duolink proximity ligation assay

The cells were cultured in 6-well plates at 37 °C overnight (initial density of 6.0×10^3 cells/well). After the transfection of nanoparticles and necrosis induction, the cells were treated with the Duolink PLA procedure according to the manufacturer's guidelines. The cells were rinsed with PBS twice, fixed with 4% paraformaldehyde for 20 min and permeabilized with Triton X-100 for 10 min. The cells were then incubated with RIP1 and RIP3 primary antibodies at 4 °C overnight, and treated with MINUS and PLUS PLA probes at 37 °C for 1 h, followed by the ligation at 37 °C for 30 min and the amplification at 37 °C for 100 min. Finally, the images were captured using LSM 710 confocal laser scanning microscope (Carl Zeiss Microscopy LLC, Jena, Germany).

2.11. RNA-sequence analysis

The cells were cultured in 6-well plates at 37 °C overnight (initial density of 6.0×10^3 cells/well), and then subjected to the transfection of nanoparticles. Intracellular RNA was extracted using NEBNext® Ultra™ RNA Library Prep Kit (*Illumina* Inc, CA, USA) according to the manufacturer's instructions. Samples were indexed, clustered and sequenced on an Illumina Novaseq platform to produce 150 bp paired-end reads. Differential expression analysis was performed using the DESeq2 R package 1.16.1, adjusting the P values for false discovery rate (FDR) using the Benjamini and Hochberg's approach. Genes with an adjusted and $|\log2(\text{FoldChange})| \geq 1$ were identified as differentially expressed. Enrichement analysis was performed using clusterProfiler for GO terms. GSEA was conducted to identify the differentially expressed gene sets based on KEGG database. Ingenuity pathway analysis (IPA) was employed to annotate pathways and biological functions, with Z-score indicating activation (>0) or inhibiton (<0).

2.12. Therapeutic treatment of collagen-induced arthritis (CIA) mice

All animal procedures were approved by the Institution Animal Ethics Committee of Jilin University (Approval Nos. 2023YNPZSY012, 2023YNPZSY013, 2022YNPZSY036, 2024YNPZSY090 and 2024YNPZSY089), and conducted in accordance with the guidelines of Care and Use of Laboratory Animal Experience of Jilin University.

Male DBA1/J mice (aged 7−8 weeks, approximately 20 g) were acquired from Beijing Vital River Laboratory Animal Technology Co., Ltd. (Beijing, China) and housed in pathogen-free environment under standard light/dark cycle (12 h/12 h). After the acclimation, the mice were subcutaneously immunized with 100 μg type II bovine collagen in 50 μL CFA containing 2 mg/mL *Mycobacterium tuberculosis* and with a booster of collagen in IFA three weeks later. The mice were randomly divided into eight groups and intravenously adminstered with saline, AP, AP/siRIP3 (0.5 mg/kg, N/P ratio of 10.0), AP/R3-Dz (0.5 mg/kg), AP/R3-iDz (0.5 mg/kg), and AP/R3-Dz (0.5 mg/kg) combined with MCC950 (10 mg/kg, intraperitoneal administration). Treatments were conducted once every 2 days for a total of 6 times post-21 days from the primary immunization. The severity of arthritis was assessed by measuring the paw thickness and clinical scores, with erythema and swelling from 0 to 4 (Supporting Information Table S3). After 44 days, the paw images were captured, and the tissues were collected for gene expression and histopathological evaluation.

2.13. Therapeutic treatment of gouty arthritis mice

Male C57/BL6J mice (aged 6−8 weeks) were obtained from Beijing Vital River Laboratory Animal Technology Co., Ltd. (Beijing, China). Monosodium urate (MSU) crystals were fabricated following a well-established procedure[29]. In brief, 0.5 g uric acid and 0.25 g NaOH were added into 50 mL distilled water and heated to 80 °C for 20 min until complete dissolution. The mixture was adjusted to pH 7.1−7.2 through the addition of HCl and further crystallized at 4 °C overnight. The precipitate was treated

with ethanol under the sonication for 30 min to achive the dispersion. Finally, the precipitate was collected by the centrifugation at 400 × *g* for 10 min and dried at 70 °C. The mice were intra-articularly injected with saline, AP, AP/siRIP3, AP/R3-Dz with 5 mmol/L $MgCl_2$ and AP/R3-iDz with 5 mmol/L $MgCl_2$. MSU crystals (3 mg in 20 μL saline) were injected into the hind paws to induce GA. Treatments were carried out 12, 24, 48 and 72 h before and 24 h after the induction of model. The mice were sacrificed after the treatment for 24 h, and their hind paws were immediately fixed in 10% formalin for subsequent analysis.

2.14. Therapeutic treatment of experimental autoimmune hepatitis mice

Male C57/BL6J mice (aged 6−8 weeks) from Beijing Vital River Laboratory Animal Technology Co., Ltd. (Beijing, China) were acclimated for one week and then randomly divided into eight groups as previously described. Acute liver injury was induced *via* intravenous injection of concanavalin A (Con A) (20 mg/kg in 100 μL saline), while a lethal dose (30 mg/kg) was used for survival experiments. The mice were randomly divided into eight groups and intravenously administered with saline, AP, AP/siRIP3 (0.5 mg/kg, N/P ratio of 10.0), AP/R3-Dz (0.5 mg/kg), AP/R3-iDz (0.5 mg/kg), and AP/R3-Dz (0.5 mg/kg) combined with MCC950 (10 mg/kg, intraperitoneal administration). Treatment was given every two days starting one week before Con A induction. The mice were sacrificed 12 h post-Con A injection to collect liver tissues and blood. The liver samples were photographed to observe macroscopic injury and subjected to the gene expression and histopathological analysis. The levels of ALT and AST in serum were measured by AU 400 automated clinical chemistry analyzer (Olympus, Tokyo, Japan).

2.15. Histopathological and immunochemical analysis

The decalcified ankle tissues and other tissues were sectioned for histological analysis including hematoxylin and eosin (H&E) staining, Safranin O/Fast Green staining and toluidine blue (TB) staining. The infiltrated cells, cartilage thickness and damage area were quantified with the Image J software v1.5j8 (National Institutes of Health, Maryland, USA). Histological synovitis scores (HSS) of hyperplastic synovium and Mankin score were assessed according to Supporting Information Tables S4 and S5. For the immunochemical analysis, tissue sections were subjected to antigen retrieval in EDTA solution in a microwave oven for 12 min. The endogenous peroxidase activity in the sections was blocked by 3% (*v*/*v*) hydrogen peroxide solution for 25 min in the dark, followed by blocking non-specific proteins with 3% (*w*/*v*) BSA solution for 30 min. The sections were incubated at 4 °C overnight in blocking buffer with the corresponding primary antibodies and then treated with the HRP-conjugated secondary antibody at room temperature for 50 min. Finally, the sections were visualized using diaminobenzidine (DAB) substrate for 10 min and counterstained with hematoxylin. All the sections were observed and photographed with Olympus DP70 microscopy (Tokyo, Japan). The positive areas with protein expression were quantified with the Image J v1.5j8 software (National Institutes of Health, Maryland, USA).

2.16. Statistical analysis

All data are presented as mean ± standard deviation (SD) of at least triplicate experiments. One-way ANOVA with LSD *post-hoc* correction was used for statistical evaluation to compare values between groups. The statistical difference between the two groups were assessed by two-tailed unpaired Student's *t*-test. All graphs and subsequent statistical analysis were performed using GraphPad Prism version 9.5.

3. Results

3.1. R3-Dz as a high-efficacy gene silencer knocked down the RIP3 expression

The inhibition of caspase-8, coupled with the activation of Toll-like receptor 4 (TLR4), can initiate the necroptosis program in macrophages[30]. Thus, we established a necroptosis model by stimulating RAW264.7 cells with LPS and caspase-8 inhibitor Z-VAD (Fig. 1A). The typical necroptotic phenotypes could be observed in the macrophages after the LPS and Z-VAD treatment, as characterized by high membrane permeability and mitochondrial swelling (Fig. 1B). This increased membrane permeability allowed propidium iodide (PI) dye to penetrate the disrupted cell membrane, marking the undergoing necroptosis. As shown in Fig. 1C and Supporting Information Fig. S1, the cells underwent necroptosis following the treatment with LPS and Z-VAD, as evidenced by obvious red fluorescence. In contrast, neither LPS nor Z-VAD elicited this response, indicating the absence of necroptosis. Consistent with these findings, a lower percentage of viable cells has been found in macrophages after the co-induction with LPS and Z-VAD, as illustrated by ATP viability assay (Fig. 1D). These findings indicated the successful establishment of the necroptosis model. In necroptosis, RIP1 and RIP3 play crucial roles, as their homodimer or oligomer interaction is necessary for the formation of necrosome complex, which facilitates the cell death process[11]. Accordingly, the expression of RIP1 and RIP3 was efficiently knocked down by siRNAs, in which PEI/siRIP3 significantly rescued the cell death while the inhibition of RIP1 did not attenuate the necroptosis (Supporting Information Fig. S2 and Fig. 1E). Our observations aligned with the hypothesis that endogenous RIP1 level is critical for the macrophage survival[30]. Moreover, inspired by the anti-necroptosis effect of siRIP3, we focused our efforts on developing an effective DNAzyme, specifically targeting *RIP3* mRNA to modulate the necroptosis pathway. The secondary structure of *RIP3* mRNA was analyzed to identify conserved loop domains, within which the AU or GU junction sites with high k_{obs} were selected as suitable candidates from DNAzyme libraries (Fig. 1F and Supporting Information Fig. S3). Subsequently, the screened DNAzymes were individually transfected into macrophages to evaluate the respective gene silencing efficiency. Among the tested DNAzymes, a notable inhibition of *Rip3* mRNA level was observed, with Dz 222 (abbreviated as R3-Dz) exhibiting the highest gene knockdown ability (Fig. 1G). In addition, we employed a single-base mutation to construct the antisense DNAzyme counterpart R3-iDz, which was capable of hybridizing to the RNA target with its binding arm, but possessed an inactive catalytic core. Clearly,

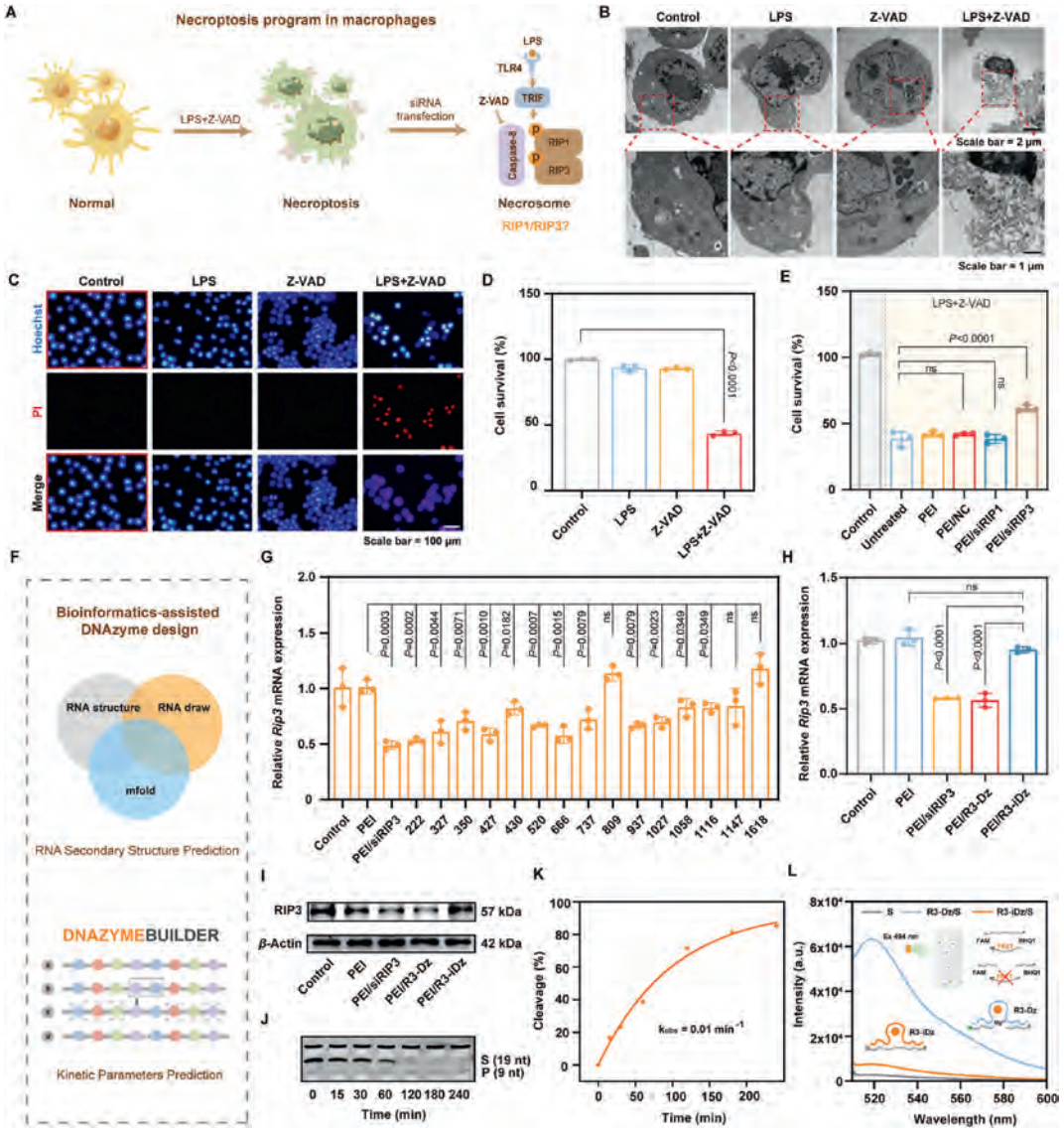

Figure 1 R3-Dz suppressed the RIP3 expression. (A) Schematic illustration for the necroptosis in macrophages. (B) Morphology of RAW264.7 cells treated with different groups by transmission electron microscopy. (C) Cell death analysis by PI/Hoechst staining. Scale bar: 100 μm. (D, E) Effect of RIP3 and RIP1 knockdown on the necropototic RAW264.7 cells by cell viability assay. (F) Schematic illustration for the bioinformatics-assisted DNAzyme design. (G) Relative *Rip3* expression in RAW264.7 cells after the treatment with the screened DNAzyme-harboring nanoparticles using qPCR. (H, I) Relative RIP3 expression in LPS and Z-VAD-stimulated RAW264.7 cells treated with different groups using qPCR and Western blotting. (J) Representative PAGE gel showing the RNA cleavage by R3-Dz. S, full-length substrate; P, cleavage product. (K) Multiple-turnover kinetic analysis of RNA cleavage by R3-Dz. k_{obs}, observed pseudo first-order rate constant. (L) Fluorescence spectra of the FRET pair-labeled mRNA substrates treated with R3-Dz and R3-iDz. Data are presented as mean ± SD (n = 3, independent experiments). One-sided statistical analysis is measured by one-way ANOVA with LSD test.

R3-iDz barely inhibited the expression of RIP3 in comparison to R3-Dz and siRIP3, indicating that the intracellular cleavage activity of R3-Dz was dependent on the conserved catalytic loop (Fig. 1H and I). Further, to verify the catalytic profile of R3-Dz, the RNA cleavage capacity was studied under multiple-turnover conditions. As shown in Fig. 1J and K, the intensity of the RNA substrate bands (19 nt) decreased in a time-dependent manner, with an observed rate constant (k_{obs}) of 0.01 min^{-1}, indicating that R3-Dz could efficiently cleave the RNA molecules. Besides, the RNA cleavage by DNAzyme was observed by FRET. As depicted in Fig. 1L, the RNA substrates were labeled with a fluorescein molecule (FAM) at the 5′ end and a quencher (BHQ-1) at the 3′ end, resulting in the fluorescence quenching due to FRET. Upon the incubation with R3-Dz, the fluorescence intensity of RNA substrates significantly increased, suggesting the separation of FRET pair due to the cleavage of RNA substrates by R3-Dz. In contrast, the lack of fluorescence intensity in the R3-iDz group implied no cleavage of RNA substrates. In addition, to investigate the substrate-specific RNA cleavage activity of R3-Dz, the RNA substrate with a single-base mutation (mut-FRET-Sub) was constructed (Supporting Information Fig. S4). No significant increase in the fluorescence intensity

of RNA substrate was observed in the R3-Dz/mut-FRET-Sub group, indicating that R3-Dz possessed excellent specificity for cleaving the RNA substrates.

To gain a deeper insight into the cleavage process and its underlying mechanism, we investigated the kinetic properties of R3-Dz/RNA complexes in both initial (R3-Dz/Substrate, R3-Dz/S) and final (R3-Dz/Product, R3-Dz/P) states of the cleavage reaction through MD simulation (Fig. 2A, Supporting Information Figs. S5−S7, Movies S1 and S2). Both complexes achieved convergence over a minimum of 30 ns, as indicated by the RMSD calculation (Supporting Information Fig. S8). The binding free energy (ΔG) analysis revealed a significantly higher value for R3-Dz/S (277.9974 kcal/mol) than R3-Dz/P (170.8004 kcal/mol). This significant difference in ΔG suggested a spontaneous and energetically favorable progression from the inital substrate state to the final product state, which meant an intrinsic propensity for the cleavage to proceed towards completion. The dG_{14} of catalytic loop has been confirmed as a key component in the RNA cleavage [28]. To further investigate the role of dG_{14} in the catalytic efficacy of R3-Dz, a targeted mutation of R3-Dz was constructed by substituting dG_{14} to dC_{14} (Fig. 2A, Supporting Information Fig. S9 and Movie S3). The R3-Dz^{G14C}/S system reached the convergence over a minimum of 30 ns, as indicated by the RMSD calculation (Fig. 2B). However, the R3-Dz^{G14C}/S system exhibited reduced structural stability compared to R3-Dz/S, as evidenced by increased RMSF values (Fig. 2C) and higher ΔG (305.5393 kcal/mol). Additionally, different from R3-Dz^{G14C}/S complex, R3-Dz/S configuration displayed a significantly shorter distance between dG_{14}-N and rA_0-$H_{O2'}$, suggesting that the dG_{14} residue in R3-Dz/S complex was crucial for the deprotonation of O2′ atom on rA_0 residue, likely facilitating the formation of precatalytic conformation necessary for the subsequent cleavage reaction (Fig. 2D). Morever, the R3-Dz/S complex exhibited a decreasing trend in the distance between the dG_{14}-N of catalytic loop and the rA_0-$H_{O2'}$ of

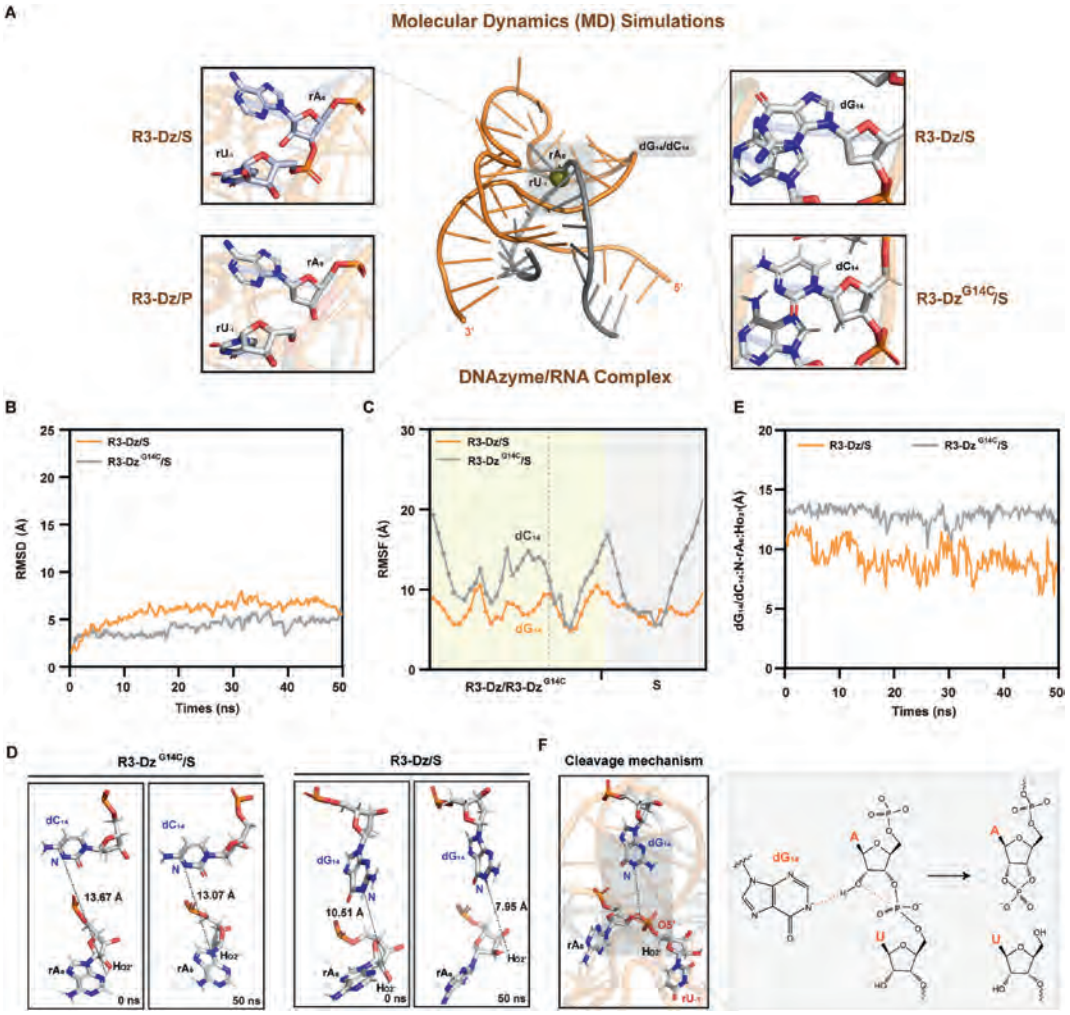

Figure 2 MD simulation of DNAzyme/RNA complexes. (A) Schematic overview of the DNAzyme/RNA complexes in the initial reaction state (R3-Dz/S), final reaction state (R3-Dz/P) and mutant state (R3-Dz^{G14C}/S) during MD simulation. (B) RMSD to analyze the system equitability. (C) RMSF to analyze the backbone stability. (D) Snapshots taken at the start (0 ns) and the end (50 ns) of MD simulation to show the distance between dG_{14}/dC_{14}-N and rA_0-$H_{O2'}$ of corresponding systems, respectively. (E) Distance between dG_{14}/dC_{14}-N and rA_0-$H_{O2'}$ measured from the MD trajectories of corresponding systems. (F) Mechanism scheme of R3-Dz-mediated RNA cleavage. The functional group of dG_{14} in the catalytic loop acts as the Brønsted base to abstract a proton from the O2′ atom of rA_0 (black dashed line), and this action facilitates an in-line attack (red dashed line) by the newly formed 2′-oxyanion on the phosphorous (P) and O5' atoms of rU_{-1}, leading to the cleavage of phosphodiester bond.

cleavage site region during the reaction (Fig. 2E). However, this spatial convergence was not replicated in the R3-Dz^{G14C}/S complex. These results suggested that the optimal alignment of dG_{14} near the cleavage site facilitated the abstraction of a proton from the O2′ atom of rA_0 residue during the cleavage reaction. Moreover, the precise positioning of dG_{14} could contribute to an in-line attack by the newly formed 2′-oxyanion on the phosphorous (P) and O5' atoms of rU_{-1}, ultimately leading to the cleavage of phosphodiester bond (Fig. 2F).

3.2. AP mediated the intracellular delivery and release of R3-Dz

To improve the transfection efficiency and stability of R3-Dz, PAMAM derivative (namely AP) was synthesized by the modification of 2-amino-6-chloropurine (Fig. 3A). According to the ^{1}H NMR spectrum of AP, the presence of characteristic peak at 7.58 ppm was attributed to the aromatic ring of 2-amino-6-chloropurine, and 35 of primary amines on the surface of PAMAM was calculated to be modified by 2-amino-6-chloropurine (Supporting Information Fig. S10). The binding and condensation capability of AP dendrimer with nucleic acids was then assessed. As shown in Fig. 3B, the AP dendrimer was able to form stable nanoparticles with R3-Dz at N/P ratios greater than 5.0, suggesting that the surface-engineered PAMAM derivative maintained the ability to compact and assemble DNAzyme molecules. As characterized by TEM, the morphology of AP/R3-Dz nanoparticles showed a spherical structure with diameter of ca. 180 nm (Fig. 3C). The hydrodynamic diameter and zeta potential of AP/R3-Dz nanoparticles also indicated that AP dendrimer could assemble with R3-Dz into a condensed structure, which was beneficial for the R3-Dz transfection (Fig. 3D and E). Notably, the modification with nucleobase analogs led to decreased zeta potential values of AP/R3-Dz compared with PAMAM/R3-Dz nanoparticles at identical N/P ratios. This alteration might lessen the interaction between nanoparticles and negatively charged components of cell membrane, thereby contributing to the reduced cytotoxicity (Fig. 3F). Subsequently, to optimize the transfection efficiency of nanoparticles in macrophages, AP and PAMAM were complexed with FAM-labelled R3-Dz at different N/P ratios. Compared with free FAM-labelled R3-Dz, green fluorescence could be observed after the treatment with AP/FAM-R3-Dz and PAMAM/FAM-R3-Dz nanoparticles, suggesting that these dendrimers were capable of mediating the intracellular delivery of R3-Dz. Particularly, the AP/R3-Dz nanoparticles exhibited stronger transfection efficiency compared to PAMAM/R3-Dz nanoparticles at identical N/P ratios (Fig. 3G−I and Supporting Information Fig. S11). While the modification shielded the positive charge density of nanoparticles, the incorporation of nucleobase analogs may tailor the binding and dissociation of carriers and nucleic acids through hydrogen bonding, thereby promoting the endocytosis and intracellular release of DNAzymes to achieve better transfection. Meanwhile, N/P ratio of 10.0 was chosen as the optimal ratio in the subsequent experiments to obtain efficient transfection and low cytotoxicity. The loading amount and encapsulation efficiency of AP/R3-Dz nanoparticles at the N/P ratio of 10.0 were 9.67% and 93.7%, respectively. The stability of the nanoparticles in the physiological environment is critical for the efficient intracellular catalytic activity of R3-Dz. AP provided efficient protection for R3-Dz against the DNase degradation (Supporting Information Fig. S12A). As shown in Fig. S12B and S12C, there was no obvious degradation of nucleic acids accompanied by only a slight increase in hydrodynamic diameter after the incubation with 10% FBS for up to 24 h, meaning that the AP/R3-Dz nanoparticles exhibited favorable serum stability. In addition, no apparent aggregation was observed over time, indicating that AP/R3-Dz nanoparticles possessed good colloidal stability and long-term stability (Supporting Information Fig. S13). Controlled drug release is a key strategy to reduce systemic side effects and increase bioavailability, and thus the release of R3-Dz from nanoparticles was monitored in different pH solutions. The AP/Cy5-R3-Dz nanoparticles showed faster release of Cy5-R3-Dz in the buffer of pH 5.5 than buffer solutions of pH 7.4 and 6.5 (Supporting Information Fig. S14). The AP/R3-Dz nanoparticles exhibited the acid-sensitive release behavior that benefited from the hydrogen bonding interaction between AP carrier and R3-Dz, thus promoting the on-demand drug release in inflammatory microenvironment. Further, the fluorescence signal of FRET-R3-Dz stabilized at the maximum intensity around approximately 36 h when it was transfected into macrophages, indicating that the intracellular level of FRET-R3-Dz could remain for a long period and then it could be gradually degraded to avoid the side effects (Supporting Information Fig. S15). Not surprisingly, the AP/R3-Dz nanoparticles displayed excellent biocompatibility, as evidenced by no significant cytotoxicity and hemolysis compared to the control group (Fig. 3J and Supporting Information Fig. S16). In addition, we studied the intracellular behavior of AP/R3-Dz nanoparticles after the endocytosis. As shown in Fig. 3K, after the endocytosis by macrophages, AP/R3-Dz nanoparticles facilitated the lysosomal escape within 8 h to protect DNAzyme molecules against the degradation in acidic environment due to the "proton sponge" effect of dendrimer. To ensure the knockdown efficiency, the RIP3 expression was determined (Fig. 3L and M). Compared with the control group, AP/R3-Dz led to a significant decrease of RIP3 expression in macrophages while AP/R3-iDz did not inhibit the expression of RIP3. These results indicated that the gene silencing effect was specifically attributed to the catalytic activity of R3-Dz, emphasizing its critical role in the targeted downregulation of RIP3 (Fig. 3N).

3.3. R3-Dz suppressed programmed necroptosis in macrophages by targeting RIP3

Having proved that AP effectively mediated the delivery of R3-Dz to inhibit the RIP3 expression, we next explored its impact on necroptosis. After the transfection with AP and AP/R3-iDz nanoparticles, cellular disturbances such as leakage and disruption of cell membrane and swelling of organelles were still evident. Conversely, the cells treated with AP/R3-Dz and AP/siRIP3 nanoparticles showed a reduction in these adverse cellular effects (Fig. 4A). Moreover, partial cell death in RAW264.7 cells could be alleviated after the transfection of AP/R3-Dz nanoparticles, as evidenced by ATP viability assay (Fig. 4B). Coordinately, a significantly decreased percentage of dead cells was observed following the transfection of AP/R3-Dz in RAW264.7 cells (Fig. 4C and D). As reported, RIP1 and RIP3 interact with each other to form the necrosome, which recruits and phosphorylates MLKL, and subsequently MLKL translocates to the cell membrane to disrupt the integrity of membrane, ultimately activating the necroptosis[11]. As shown in Fig. 4E and F, there was an obvious interaction signal between RIP1 and RIP3 in necroptotic cells, meaning their involvement in the necroptosis process. Remarkably, the transfection of AP/R3-Dz nanoparticles

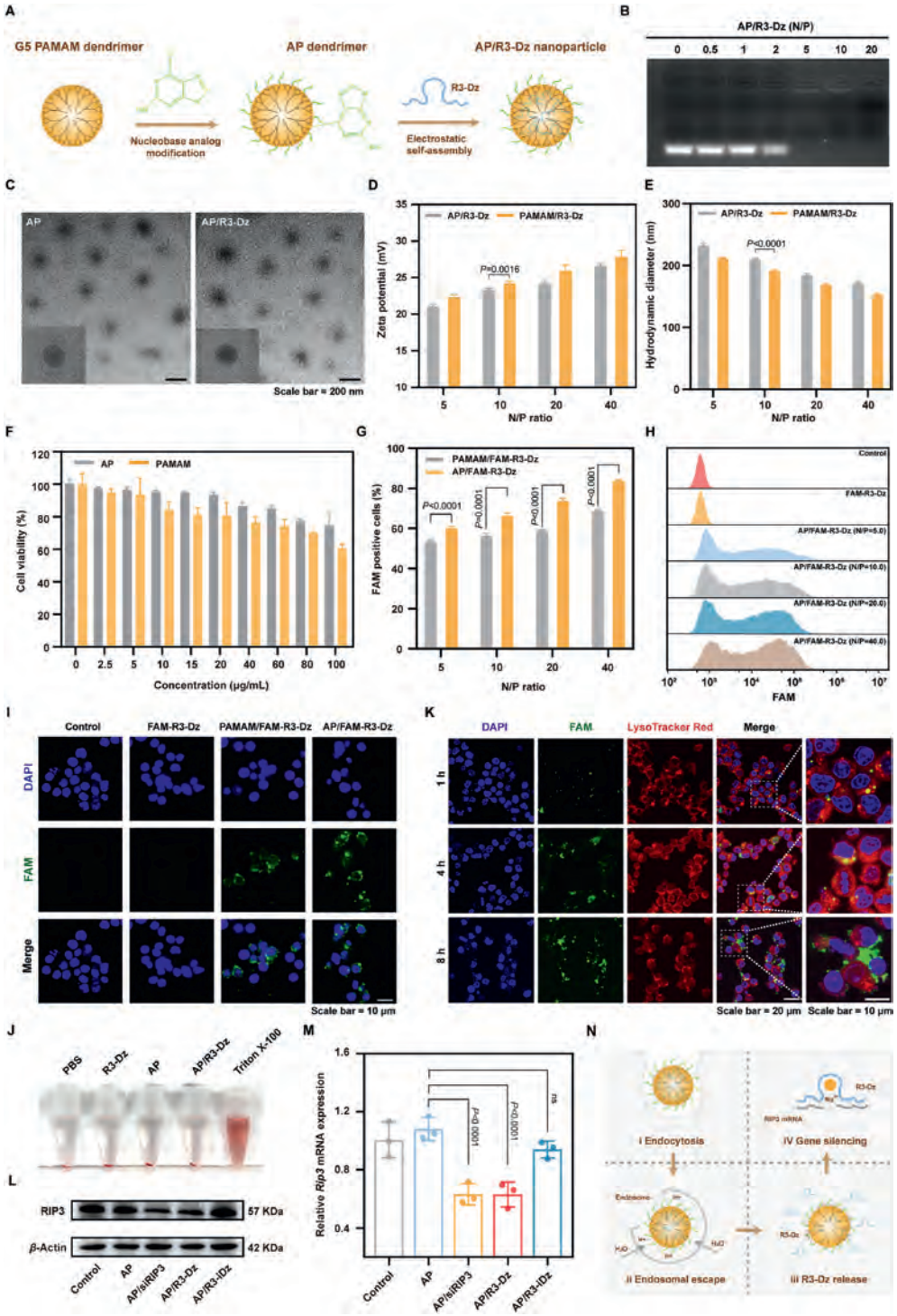

Figure 3 AP mediated the intracellular delivery and release of R3-Dz. (A) The construction of AP/R3-Dz nanoparticles. (B) The binding and condensation ability of AP dendrimer with R3-Dz at different N/P ratios. (C) Representative TEM images of AP dendrimer and AP/R3-Dz nanoparticles. Scale bar: 200 nm. (D, E) Zeta potential and hydrodynamic diameter of dendrimer/R3-Dz nanoparticles. (F) Cytotoxicity analysis of RAW264.7 cells treated with dendrimers for 48 h. (G, H) Cellular uptake efficiency of dendrimer/FAM-R3-Dz nanoparticles at different N/P ratios using flow cytometry. (I) Fluorescence images of the dendrimer-mediated FAM-R3-Dz transfection in RAW264.7 cells at N/P ratio of 10.0. Scale bar: 10 μm. (J) Hemolysis assay of red blood cells after the treatment with different groups; Triton X-100 (positive control), PBS (negative control). (K) The endosomal escape visualized by confocal laser scanning microscopy after the transfection of nanoparticles at 1, 4 and 8 h. Blue, DAPI; green, FAM-R3-Dz; red, LysoTracker Red. (L, M) Relative RIP3 expression in LPS and Z-VAD-stimulated RAW264.7 cells treated with different groups using qPCR and Western blotting. (N) The endocytosis process of the AP-mediated R3-Dz delivery. The AP/R3-Dz nanoparticles were uptaken by the macrophages, escaped from the endosomes and further released R3-Dz in the cytoplasm to target *RIP3* mRNA, leading to the inhibition of RIP3 expression. Data are presented as mean ± SD ($n = 3$, independent experiments). One-sided statistical analysis is measured by one-way ANOVA with LSD test. Comparisons between two experimental groups are performed by two-tailed unpaired Student's *t*-test.

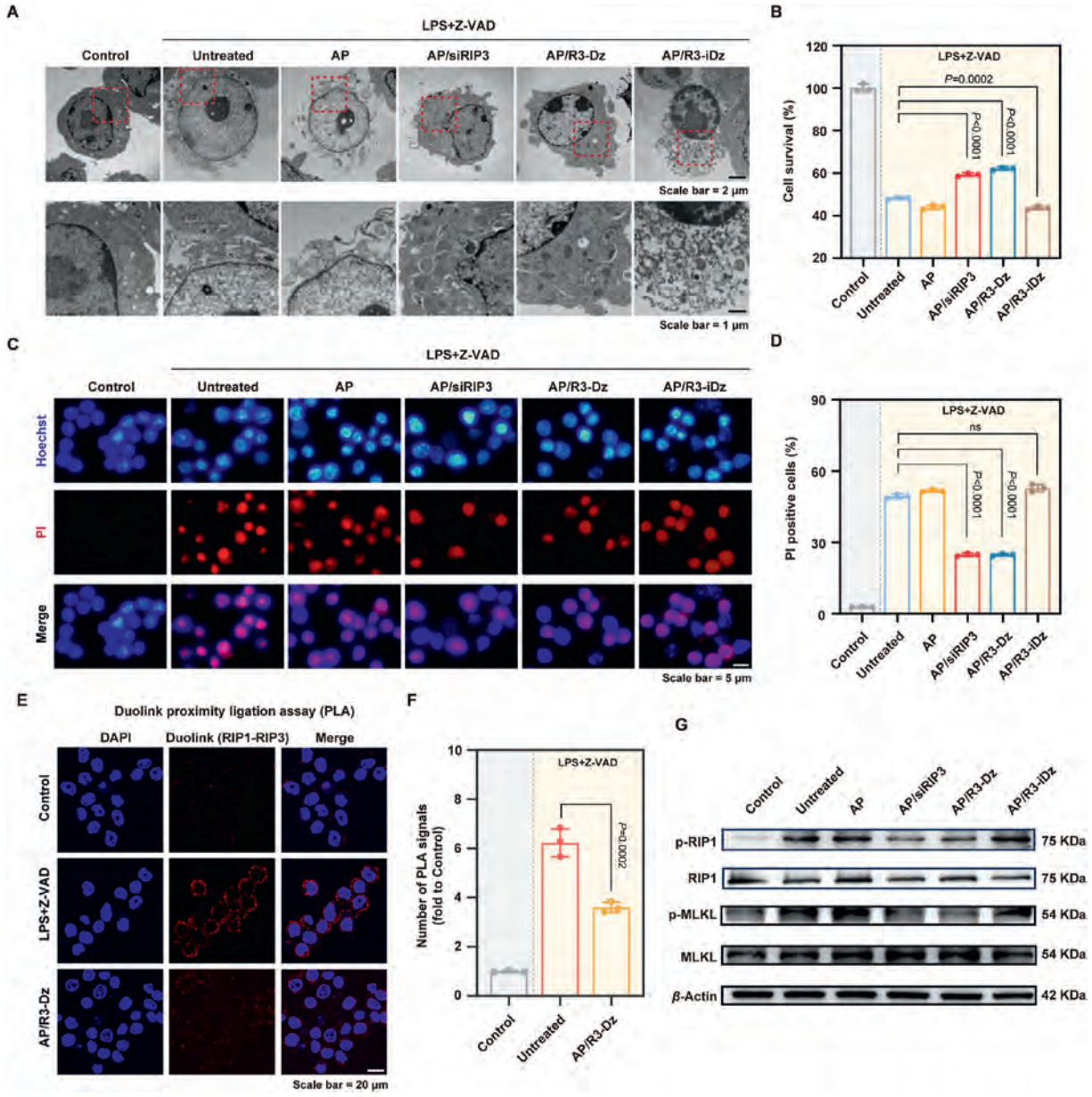

Figure 4 R3-Dz inhibited the necroptosis in macrophages. (A) Morphology of RAW264.7 cells treated with different groups by transmission electron microscopy. (B) Cell viability assessment after the treatment with different groups by CellTiter-Glo. (C, D) Cell death assessment after the treatment with different groups by PI/Hoechst staining. Scale bar: 5 μm. (E, F) Duolink assay showing the interaction of endogenous RIP1 and RIP3 in RAW264.7 cells. Histogram: quantitation of the number of PLA-positive signals (red). Scale bar: 20 μm. (G) The protein expression level of phosphorylated RIP1 and MLKL after the treatment with different groups assessed by Western blotting. Data are presented as mean ± SD (n = 3, independent experiments). One-sided statistical analysis is measured by one-way ANOVA with LSD test. Comparisons between two experimental groups are performed by two-tailed unpaired Student's t-test.

clearly declined the PLA signal, suggesting that the interaction of RIP1 and RIP3 in macrophages has been strongly inhibited by AP/R3-Dz nanoparticles. Moreover, RIP1 and MLKL phosphorylation increased following the LPS and Z-VAD stimulation in comparison to the control group (Fig. 4G and Supporting Information Fig. S17). Meanwhile, there were no obvious changes in the expression of p-RIP1 and p-MLKL in the macrophages treated with AP or AP/R3-iDz. Conversely, a substantial decrease of p-RIP1 and p-MLKL was observed after the treatment with AP/R3-Dz, suggesting that the nanoparticles harboring R3-Dz exhibited a strong inhibition on the necroptotic effectors. These results demonstrated that AP/R3-Dz nanoparticles disrupted the necroptotic signaling pathway by silencing RIP3, eventually preventing the progression of cell death.

3.4. R3-Dz negatively regulated necroinflammation by inhibiting the NLRP3 signaling pathway

Necroinflammation is widely recognized as a vigorous inflammatory response associated with necroptosis, forming a self-

amplifying feedback loop that continually escalates the inflammatory process. To further elucidate the detailed mechanism of necroinflammation, RNA-seq analysis was performed to determine the gene expression profiles and pathways activated during this process, revealing key regulatory genes and molecular interaction involved in driving the necroinflammatory responses. A total of 6903 differentially expressed genes (DEGs) were identified between control and necroptotic cells (treated with LPS and Z-VAD), among which 3804 genes were upregulated and 3099 genes were downregulated (Supporting Information Fig. S18). Gene Ontology (GO) analysis of DEGs revealed that the treatment with LPS and Z-VAD primarily induced the expression of genes associated with inflammatory response, cytokines' production and programmed cell death, suggesting that the necroptotic cells were undergoing the inflammation (Fig. 5A). Conversely, the treatment with AP/R3-Dz nanoparticles led to a decreased expression of genes involved in inflammation response (*Il6*, *Ccl2*) and NLRP3 inflammasome complex assembly (*Tlr4*, *Nlrp3*) in necroptotic cells (Fig. 5B). Further, IPA of these DEGs offered deeper insights into the dynamic molecular signatures, as depicted in Fig. 5C. In addition to the immune response (such as IL-6 and macrophage activation signaling pathways) and necroptosis signaling pathways, there was significant enrichment in HMGB1 signaling pathway and production of nitric oxide and ROS. Thus, we analyzed the expression of HMGB1 and ROS released from the necrotic cells (Fig. 5D−F, Supporting Information Figs. S19 and S20). HMGB1, as known DAMPs released from necrotic cells, triggers an inflammatory response by interacting with receptors such as TLRs, thereby initiating a cascade of inflammatory events[31]. Upon stimulation with LPS and Z-VAD, macrophages exhibited a significant increase in HMGB1 level, whereas the treatment with AP/siRIP3 nanoparticles resulted in a marked decrease in HMGB1 expression. The results indicated that the release of HMGB1 was strongly influenced by RIP3 in necrotic macrophages (Fig. 5D). Besides, ROS plays a role in executing necroptotic cell death and exacerbating inflammation, primarily by increasing oxidative stress and causing biomolecular damage. As shown in Fig. 5E and F, Supporting Information Figs. S19 and S20, necroptosis induced the generation of total cellular ROS and mitochondria-derived ROS, as evidenced by strong fluorescence signals in macrophages, whereas the treatment with AP/siRIP3 nanoparticles led to the inhibition of total cellular ROS and mitochondria-derived ROS levels, also illustrating that ROS induction was dependent on the necrosomal RIP3. Notably, AP/R3-Dz nanoparticles showed effective inhibition of HMGB1, total cellular ROS and mitochondria-derived ROS generation, with comparable efficacy to AP/siRIP3. Considering the pivotal roles of HMGB1 and ROS in priming and activating the NLRP3 inflammasome, we aimed to investigate whether necroptosis was involved in the activation of NLRP3 inflammasome and consequently influenced the progression of inflammation[32]. GSEA strongly implicated NOD-like receptor, Toll-like receptor and NF-κB signaling pathways as the biological processes affected by LPS and Z-VAD induction, suggesting that the initiation of inflammatory pathways potentially led to the NLRP3 inflammasome activation (Fig. 5G and Supporting Information Fig. S21). The upregulation of NLRP3 expression following the stimulation with LPS and Z-VAD suggested a role of necroptosis in the activation of NLRP3 inflammasome (Fig. 5H). This activation typically involves key biochemical events, such as the cleavage of procaspase 1 and subsequent release of inflammatory cytokines IL1β and IL18. The necroptosis significantly increased the expression of *caspase-1*, *Il1β* and *Il18* (Fig. 5I), corroborating the involvement of necroptotic pathways in promoting the NLRP3 inflammasome-mediated inflammatory responses. Transfection with AP/siRIP3 nanoparticles not only led to a downregulation of NLRP3 expression but also reduced the secretion of pro-inflammatory cytokines, indicating the RIP3's pivotal role in modulating the NLRP3 inflammasome pathway to drive necroinflammation (Fig. 5H and Supporting Information Fig. S22). Following the R3-Dz delivery, marked reduction in the expression of NLRP3 and pro-inflammatory cytokines has been observed, demonstrating the anti-inflammatory potential of AP/R3-Dz in macrophages undergoing necroptosis (Figs. 5J, 6A−D, and Supporting Information Fig. S23). These findings meant that necroptosis promoted the NLRP3-mediated inflammation *via* RIP3, and AP/R3-Dz nanoparticles effectively counteracted the activation of NLRP3 inflammasome, thereby attenuating the inflammatory response. Taken together, necroptosis was involved the formation of a necrosome comprising RIP1 and RIP3, leading to the formation of MLKL pores in the cell membrane and the activation of excessive ROS. Subsequently, DAMPs such as HMGB1 were released through the broken cell membrane, thereby achieving the activation of TLRs. DAMPs and ROS led to the activation of NF-κB pathway and the formation of NLRP3 inflammasome to imitate the secretion of pro-inflammatory cytokines. These cytokines, in turn, further promoted the necroptosis, reinforcing the necroinflammatory loop. The AP/R3-Dz nanoparticles effectively inhibited the RIP3 expression and necrosome formation to reduce the necroptosis and counteract the activation of NLRP3 inflammasome, ultimately attenuating the inflammatory response (Fig. 6E). Further, the disease terms associated with DEGs from necroptotic cells suggested that AP/R3-Dz nanoparticles could inhibit autoimmune and other inflammatory diseases (Fig. 6F and G). All these data indicated that AP/R3-Dz nanoparticles held the potential to be used as an agent for treating inflammatory conditions.

3.5. Local delivery of R3-Dz ameliorated the inflammation in a GA mice model

Acute GA is a disease resulting from intra-articular deposition of uric acid crystals due to impaired purine metabolism and uric acid excretion. These crystals are considered to induce severe inflammation by activating both necroptosis and NLRP3 inflammasome pathways[33]. Thus, we established a mice model of acute GA by injecting MSU crystals into the joints to study the therapeutic efficacy of R3-Dz *via* intra-articular injection (Fig. 7A). The upregulation of RIP1, RIP3 and NLRP3 was confirmed in inflamed ankle samples, providing evidence that the NLRP3-mediated necroinflammation may be involved in the pathogenesis of GA (Fig. 7B). Moreover, mononuclear macrophages were actively recruited to synovial lesion sites in the GA model, where they proliferated extensively and mediated a cascade of inflammatory reaction. We consequently hypothesized that synovial macrophages might be one of primary cell types mediating necroinflammation in inflamed joints. As anticipated, in comparison to healthy mice, macrophages in the inflamed joints of GA model showed synovial hyperplasia accompanied by substantial macrophage infiltration (Fig. 7C and Supporting Information Fig. S24). Additionally, phosphorylation of RIP1, RIP3 and MLKL was observed, indicating that accumulated macrophages in synovial lesions exhibited necroptotic phenotypes to potentially exacerbate the process of disease. Subsequently, the AP/R3-Dz nanoparticles

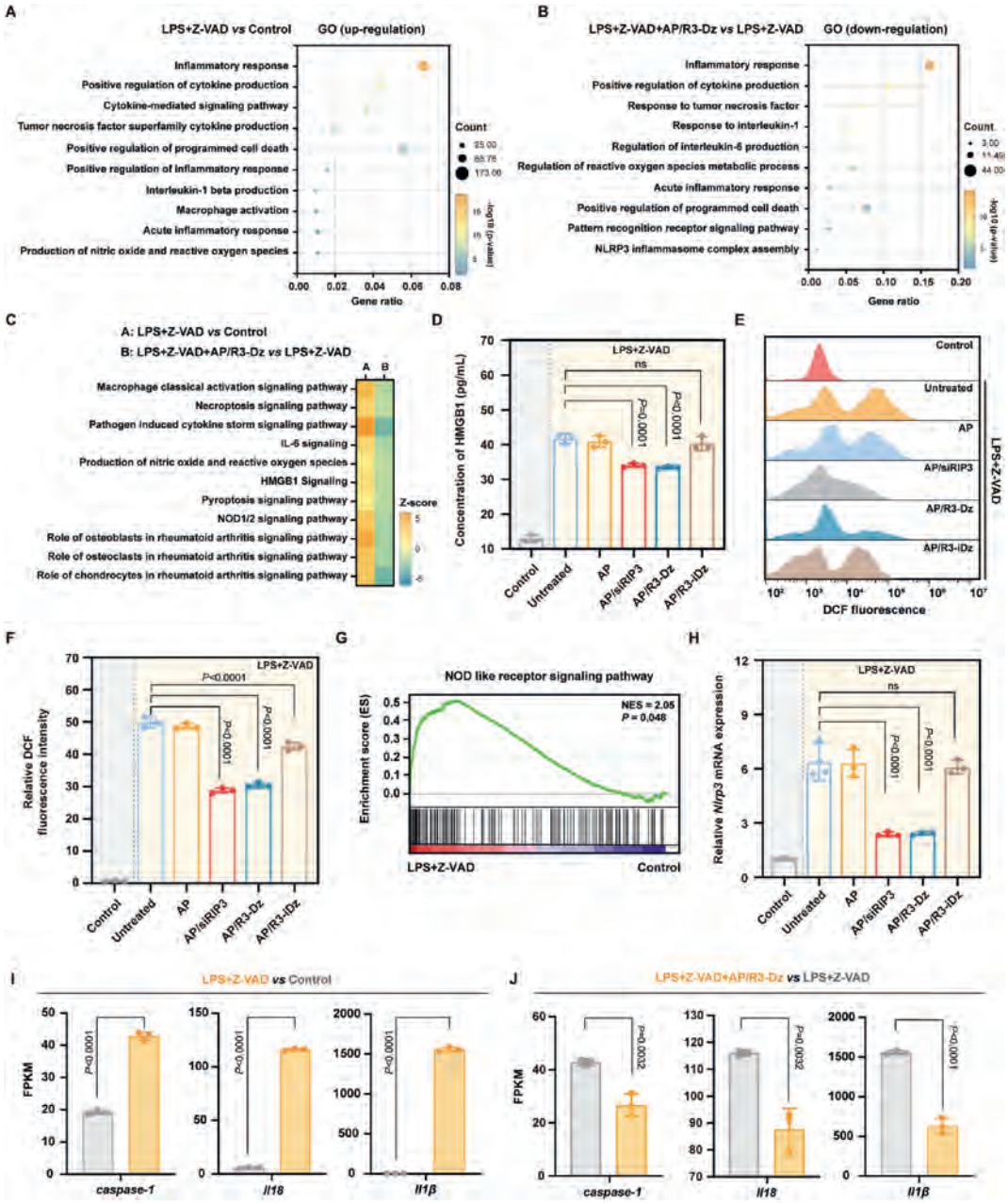

Figure 5 R3-Dz negatively regulated necroinflammation by inhibiting the NLRP3 signaling pathway. (A, B) Bubble plot for visualizing enriched GO pathway analyses of DEGs through the comparison of two groups. The higher the gene ratio, the greater the degree of enrichment. The size of the dots represents the number of genes in this GO term, and the color of the dots corresponds to different *P* value ranges. (C) IPA analysis was utilized to explore the cell signaling pathways containing DEGs between two groups, which were colored by Z-score with positive and negative scores representing the activation and inhibition. (D) HMGB1 levels in cell culture supernatant detected by ELISA. (E, F) Intracellular ROS level measured by flow cytometry after the DCF-DA staining. (G) GSEA enrichment analysis of DEGs *via* KEGG biological process database, which was presented as normalized enrichment scores (NES), false discovery rate (FDR)-corrected *P* values. (H) Intracellular expression of *Nlrp3* detected by qPCR. (I, J) Relative expression (fragment per kilobase of exon per million, FPKM) of caspase-1, *Il18* and *Il1β* in different groups. Data are presented as mean ± SD ($n = 3$, independent experiments). One-sided statistical analysis is measured by one-way ANOVA with LSD test. Comparisons between two experimental groups are performed by two-tailed unpaired Student's *t*-test.

were locally injected into the ankle joints of GA model to examine their therapeutic efficacy. Following MSU injection, the paws of GA mice progressively swelled, peaked at 6 h and persisted for at least 48 h (Fig. 7D). The administration of saline, AP and AP/R3-iDz nanoparticles did not alleviate the symptoms of swelling and inflammation, indicating that these treatments did not attain therapeutic efficacy. In contrast, AP/siRIP3 and AP/R3-Dz nanoparticles effectively suppressed the paw swelling. This reduction was also visually corroborated by representative photographs of the ankle joints taken before sacrifice, aligning with the quantitative data observed (Fig. 7E). Moreover, synovial hyperplasia and inflammatory cell infiltration, along with minor cartilage fibrosis,

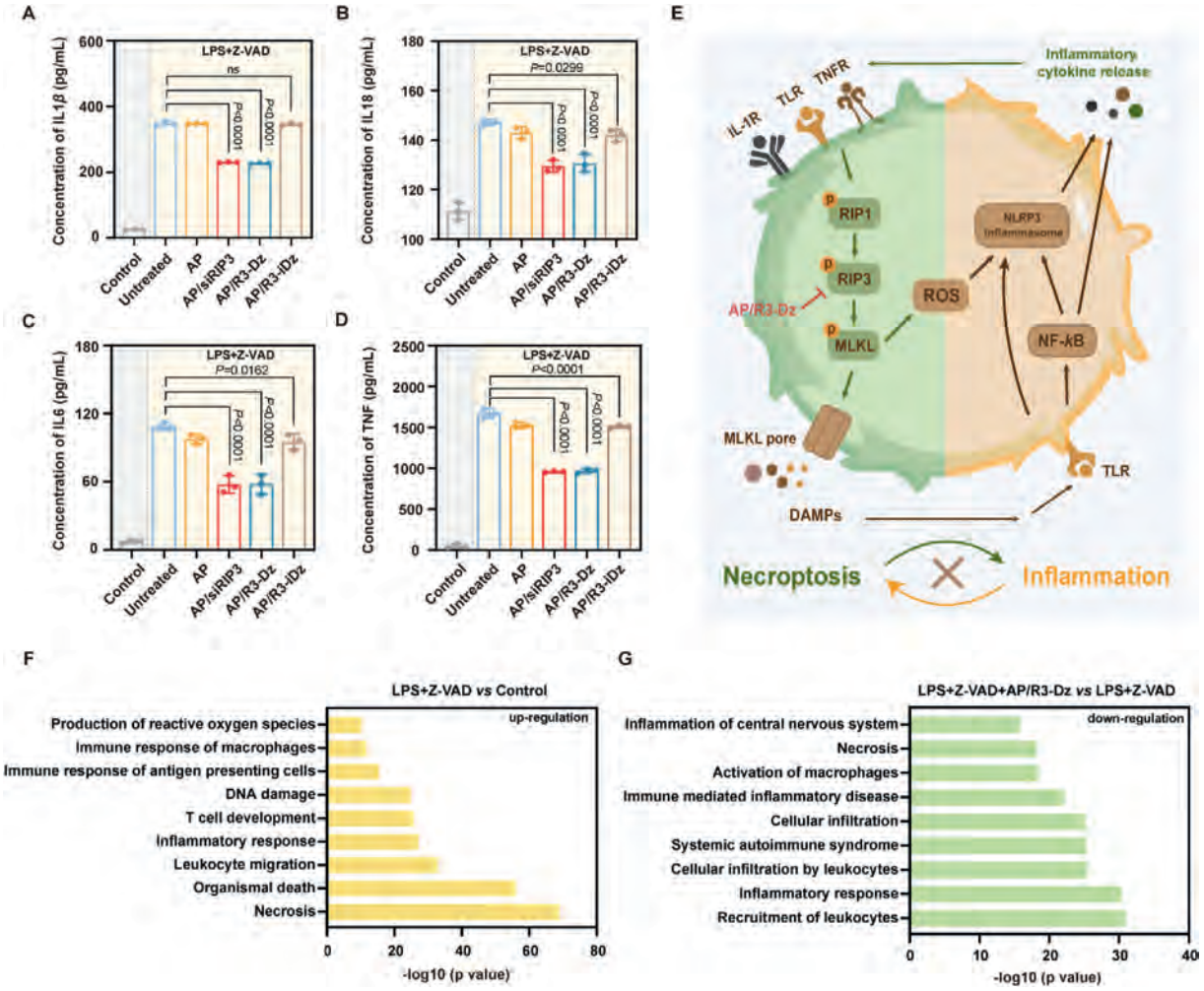

Figure 6 R3-Dz achieved the negative regulation of necroinflammation through attenuating the NLRP3 signaling pathway. (A−D) The levels of IL1β, IL18, IL6 and TNF in cell culture supernatant detected by ELISA. (E) The illustration for the anti-necroinflammation of R3-Dz by inhibiting the NLRP3 signaling pathway. The ROS and HMGB1 secreted by necroptotic macrophages accelerated the activation of NLRP3 signaling pathway to promote the production of inflammatory cytokines, which formed a feedback loop to strengthen the necroinflammation. The downregulation of RIP3 level by AP/R3-Dz nanoparticles could block the loop and further reduce the NLRP3-mediated necroinflammation. (F, G) IPA disease and function analysis of DEGs in different groups. Upregulated (Z-score>0) or downregulated (Z-score<0) terms were represented as the activation or inhibition, respectively. Data are presented as mean ± SD (n = 3, independent experiments), and one-sided statistical analysis is measured by one-way ANOVA with LSD test.

were noted in the inflamed ankles of GA mice (Fig. 7F). Treatments with saline, AP and AP/R3-iDz showed minimal impact on these pathological changes. In contrast, AP/R3-Dz nanoparticles demonstrated a protective effect against inflammatory invasion in the synovium. The findings indicated that AP/R3-Dz nanoparticles effectively mitigated the paw swelling and pathological damage of GA. Considering the therapeutic efficacy of AP/R3-Dz nanoparticles in GA model, we subsequently focused on elucidating the potential mechanism underlying the therapeutic effect, particularly in the regulation of necroptosis and inflammatory process. In the GA model, the synovium of arthritic joints displayed an active necroptotic process, evidenced by elevated levels of RIP3 and its phosphorylation, as well as increased HMGB1 expression (Fig. 7G and Supporting Information Figs. S25−S28). Remarkably, the treatment with AP/R3-Dz nanoparticles not only lowered the expression and phosphorylation of RIP3 but also effectively suppressed the HMGB1 level in the hyperplastic synovium. In addition, the detection of DCF-DA probe by *in vivo* imaging was utilized as an indicator of ROS level. The inflamed paws of GA mice were indeed in a state of oxidative stress, as evidenced by the high level of ROS (Fig. 7H and Supporting Information Fig. S29). The administration of saline, AP and AP/R3-iDz nanoparticles did not reduce the fluorescence signal of DCF-DA. In particular, the AP/R3-Dz nanoparticles showed excellent antioxidative effect, as indicated by the reduction of ROS level. Taken together, these effects indicated that the delivery of R3-Dz led to a significant reduction in necroptosis within the hyperplastic synovium of GA mice. Moreover, the NLRP3 expression level was assessed in the hyperplastic synovium of GA mice, as depicted in Supporting Information Figs. S30 and S31. Treatments with saline, AP and AP/R3-iDz did not yield a significant decrease in NLRP3 expression, whereas both AP/R3-Dz and AP/siRIP3 nanoparticles demonstrated a partial reduction in NLRP3 expression. Additionally, we evaluated the expression

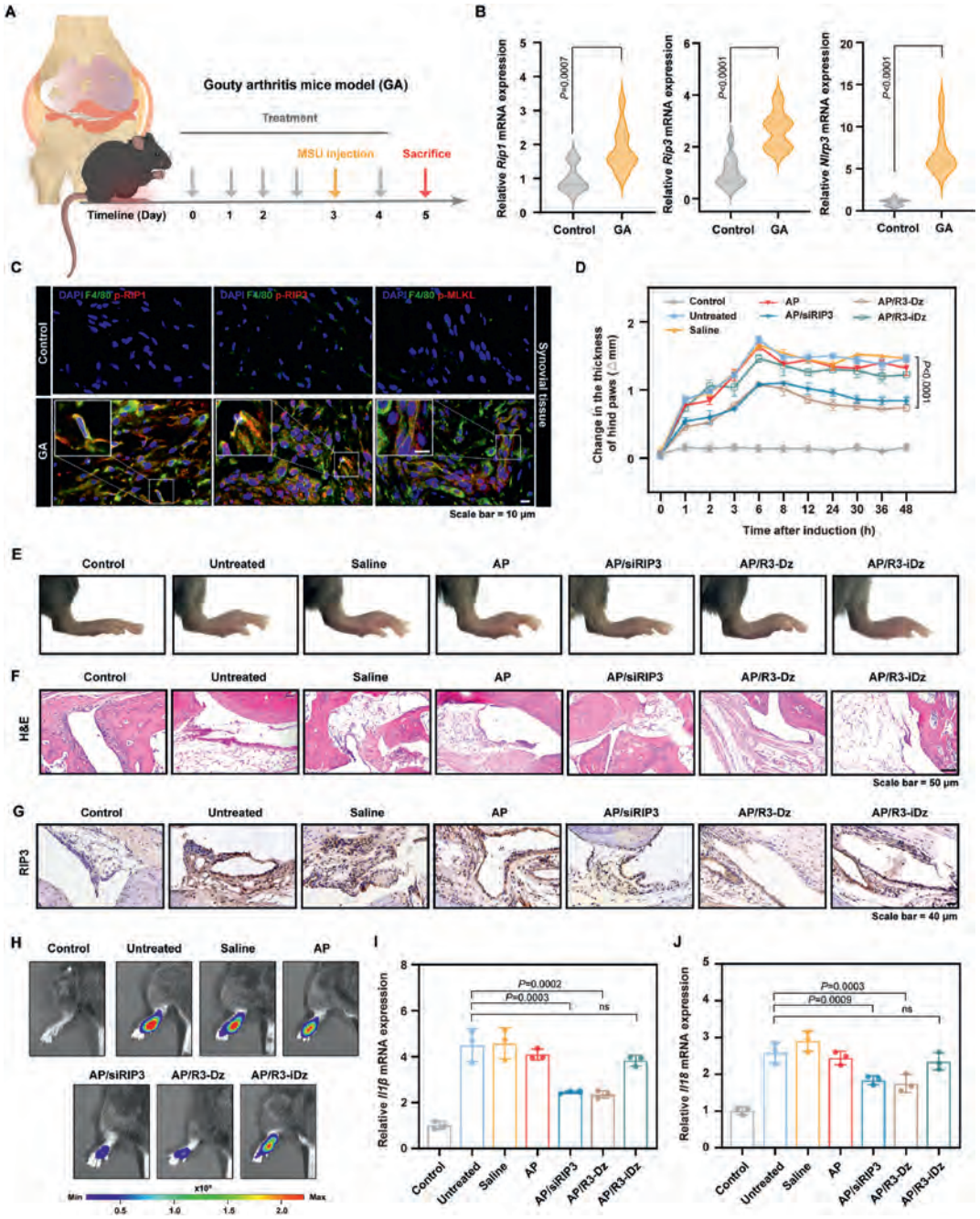

Figure 7 Local delivery of R3-Dz ameliorated the inflammation in GA mice model. (A) Schematic diagram for the establishment of GA mice and the treatment procedure. (B) The *Rip1*, *Rip3* and *Nlrp3* mRNA levels in the synovial tissues from normal and GA mice detected by qPCR ($n = 10$). Comparisons between two experimental groups are performed by two-tailed unpaired Student's *t*-test. (C) Multiplex immunofluorescence staining of synovial tissues in normal and GA mice employing macrophages (F4/80) and necrotic markers (p-RIP1, p-RIP3 and p-MLKL). Scale bar: 10 μm. (D) The thickness of hind paws during the period of 48 h post-MSU induction ($n = 5$). (E) The macroscopic observation to assess the severity of soft tissue swelling at 48 h post-MSU induction ($n = 5$). (F) Histological changes of ankle joints analyzed by H&E staining ($n = 5$). Scale bar: 50 μm. (G) RIP3 expression in arthritic joints detected by immunochemistry ($n = 5$). Scale bar: 40 μm. (H) *In vivo* fluorescence images of ROS in arthritic joints of GA mice with different treatments ($n = 5$). (I, J) Relative *Il1β* (I) and *Il18* (J) level in the synovial tissues of GA mice measured by qPCR ($n = 3$). Data are presented as mean ± SD, and one-sided statistical analysis is measured by one-way ANOVA with LSD test (D, I and J).

level of inflammatory cytokines in inflamed ankles. Notably, AP/R3-Dz and AP/siRIP3 nanoparticles showed a significant decrease in the inflammatory response, suggesting an anti-inflammatory effect of R3-Dz (Fig. 7I and J, Supporting Information Fig. S32). In summary, the observed effects of AP/R3-Dz nanoparticles in the GA model clearly demonstrated their ability to mitigate the NLRP3-mediated inflammatory response through the inhibition of necroptosis. The results aligned with and reinforced

the hypothesis of a critical interaction between necroptosis and NLRP3 inflammasome in the pathogenesis of GA. The significant decrease in RIP3 expression within the synovium and the subsequent reduction in necroinflammatory effects by R3-Dz nanoparticles, highlighted the potential of these nanoparticles as a therapeutic option to treat GA.

3.6. R3-Dz and MCC950 combination protected against liver necrosis in experimental autoimmune hepatitis (AIH)

To explore broader therapeutic potential of R3-Dz, we next expanded our research to a model of autoimmune hepatitis (AIH). This expansion into AIH capitalized on the known propensity of nanoparticles to accumulate in the liver after systemic administration, aligning with the specific needs of liver-targeted therapy. AIH, characterized by the immune-mediated destruction of hepatocytes leading to fibrosis and cirrhosis[34], presented a distinct pathological context to assess the effectiveness of R3-Dz. Thus, we developed a concanavalin A (Con A)-induced hepatitis model to further study the therapeutic potential of R3-Dz in autoimmune liver disease (Fig. 8A). In the Con A-induced hepatitis model, acute liver injury in mice was characterized by a significant increase in the expression of RIP1, RIP3 and NLRP3 within hepatic necrotic regions compared to healthy mice. This pronounced upregulation highlighted the role of necroptosis as a key driver of liver inflammation and injury, closely associated with the activation of NLRP3-based inflammatory response (Fig. 8B and C, Supporting Information Figs. S33 and S34). Recognizing the critical role of NLRP3 upregulation in liver inflammation and injury, MCC950, a selective inhibitor of NLRP3 inflammasome was integrated to augment the effects of R3-Dz, aiming at a more comprehensive treatment in AIH by simultaneously targeting distinct but interrelated pathways involved in the disease's pathology. Liver tissue in hepatitis-bearing mice exhibited significant fibrosis, necroptosis and widespread inflammatory cell infiltration (Fig. 8D−F, Supporting Information Figs. S35 and S36). The injury area has been reduced to 24.7% and 22.3% after the treatment with AP/R3-Dz and AP/siRIP3 nanoparticles, respectively. The combination of AP/R3-Dz with MCC950 showed superior effectiveness, further diminishing the extent of liver injury to near normal level. The results highlighted the enhanced therapeutic potential of the combined AP/R3-Dz and MCC950 treatment. Biochemical assays evaluating liver function revealed higher aspartate aminotransferase (AST) and alanine aminotransferase (ALT) levels in hepatitis-bearing mice treated with saline, AP and AP/R3-iDz, indicating the presence of hepatic dysfunction (Fig. 8G and H). In contrast, the mice treated with AP/siRIP3 and AP/R3-Dz exhibited reduced ALT and AST levels, showing the upgradation of liver function. Notably, the combination of AP/R3-Dz with MCC950 demonstrated a more substantial recovery of liver function, effectively restoring the balance of liver metabolism. Survival analysis revealed that the treatment with AP/siRIP3 and AP/R3-Dz improved the survival rate of hepatitis-bearing mice to 40% (Supporting Information Fig. S37). The combination of AP/R3-Dz with MCC950 markedly enhanced the survival, elevating it to 80%. These data indicated the potent therapeutic efficacy of AP/R3-Dz in reducing mortality associated with hepatitis, especially when combined with MCC950.

To elucidate the underlying mechanism, we next evaluated the distribution of AP/R3-Dz nanoparticles in control and Con A mice within 24 h (Fig. 8I). It is notable that the accumulation of Cy5-labeled R3-Dz in the inflammatory liver was significantly higher than that in the liver of control mice, indicating that the intravenous injection of AP/R3-Dz nanoparticles could passively distribute into the inflammatory liver by extravasation through leaky vasculature and subsequent inflammatory cell-mediated sequestration (ELVIS) effect. This targeted accumulation implied the effective delivery of therapeutic agent to the inflamed sites. Moreover, the treatment with AP/R3-Dz nanoparticles resulted in a significant decrease in the levels of RIP3, HMGB1 and ROS in the inflamed liver, signifying the inhibition of necroptosis pathway and the suppression of downstream effectors (Figs. 8J and 9A and B, Supporting Information Figs. S38 and S39). The combination of AP/R3-Dz with MCC950 enhanced this inhibitory effect, suggesting that the anti-inflammatory properties of MCC950 complemented the action of R3-Dz and led to a more pronounced reduction in necroptotic activity within the inflamed liver. This effect was further supported by the *in vivo* analysis of NLRP3-dependent inflammation. Treatments incorporating R3-Dz notably reduced the NLRP3 expression, and the AP/R3-Dz and MCC950 combination exhibited more profound suppression on its level (Fig. 9C and Supporting Information Fig. S40). This marked decrease supported the substantial influence of the combined treatment on NLRP3 signaling pathway. Further, the evaluation of pro-inflammatory cytokines in serum and liver tissues showed elevated levels of IL6, IL1β, TNF and IL18 in Con A-treated mice (Fig. 9D−G and Supporting Information Fig. S41). However, the treatment with R3-Dz nanoparticles effectively mitigated this inflammatory response. Notably, the combined administration of AP/R3-Dz and MCC950 showed a superior anti-inflammatory effect, as indicated by much lower level of these cytokines.

To further evaluate the type of interaction effect of AP/R3-Dz nanoparticles and MCC950, the Q value was calculated by the inhibition ratio of AST and *Tnf* levels after the treatment with different groups (Supporting Information Fig. S42). Surprisingly, AP/R3-Dz and MCC950 showed an additivity effect, with $0.85 < Q < 1.15$ for both AST ($Q = 0.97$) and *Tnf* levels ($Q = 1.10$). Finally, the biocompatibility of different formulations was evaluated, in which both AP/R3-Dz nanoparticles and the combined therapy did not induce systemic toxicity, as characterized by normal biomarkers of hepatic and renal function (Supporting Information Fig. S43). Additionally, histopathological analysis of major organs revealed no signs of organ damage or significant toxicity, further confirming the *in vivo* safety profile of these therapeutic agents (Supporting Information Fig. S44). Collectively, our findings elucidated that the combination of AP/R3-Dz and MCC950 offered an enhanced inhibitory effect on the NLRP3-mediated necroinflammation in a liver injury model. This strategy not only reduced the inflammation but also facilitated the repair of liver tissues, demonstrating its potential in the multifaceted clinical management of autoimmune hepatitis.

3.7. R3-Dz and MCC950 combination averted the articular damage in experimental RA

RA is a chronic autoimmune disease characterized by localized synovial hyperplasia, cartilage erosion, and bone destruction in joints, which progressively affects the whole body and leads to a range of intractable comorbidities. The involvement of necroptosis and NLRP3 inflammasome has been increasingly recognized in regulating the RA development, highlighting a complex interplay between cellular death pathways and inflammatory responses in its pathogenesis[35]. The expression of RIP1, RIP3 and NLRP3 was

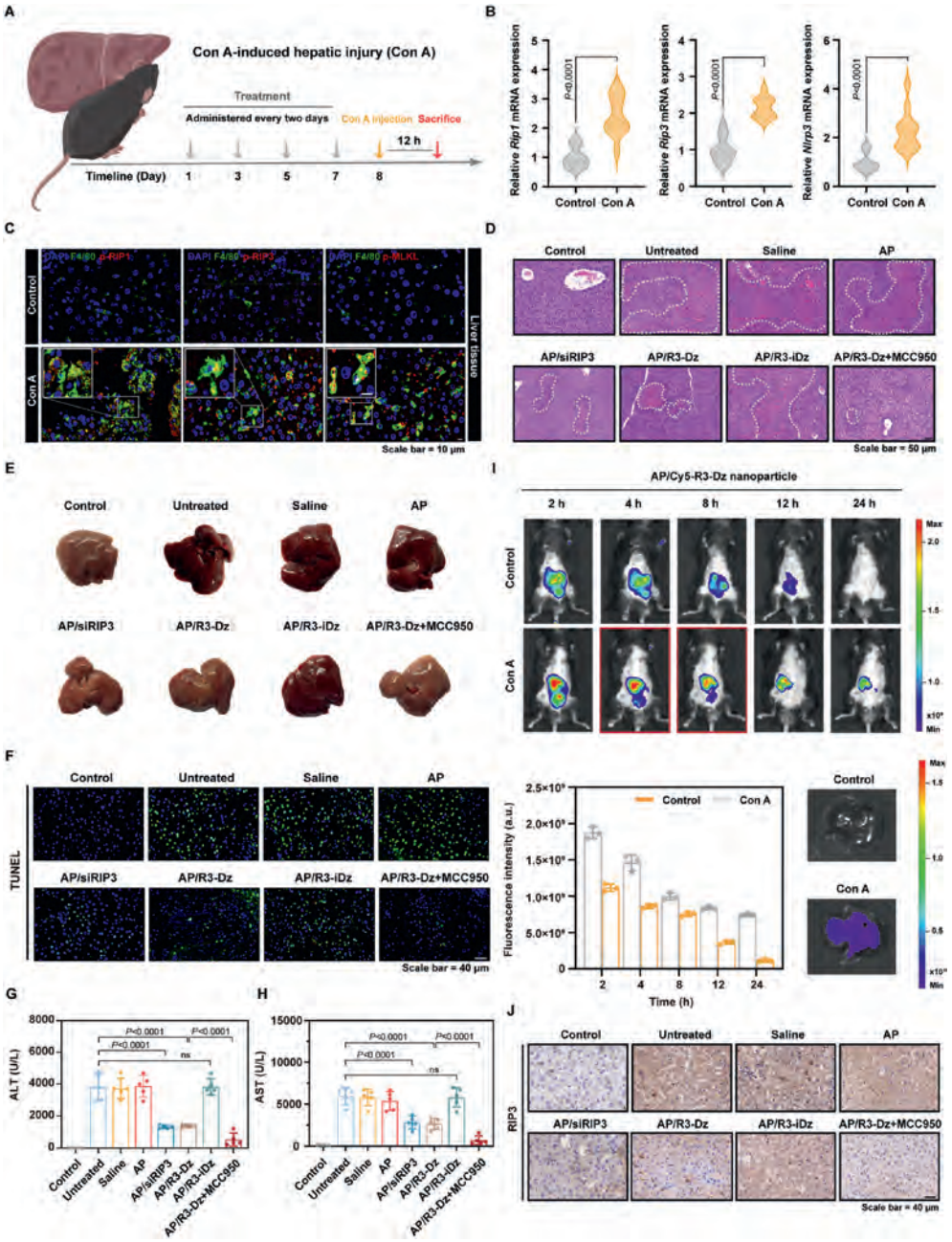

Figure 8 R3-Dz and MCC950 combination protected against the liver necrosis in experimental AIH. (A) Mice model of Con A-induced hepatic injury (Con A) and the treatment protocol. (B) The *Rip1*, *Rip3* and *Nlrp3* mRNA levels in the liver tissues from normal and Con A mice detected by qPCR ($n = 10$). Comparisons between two experimental groups are performed by two-tailed unpaired Student's *t*-test. (C) Multiplex immunofluorescence staining of liver tissues in normal and Con A mice using macrophages' (F4/80) and necrotic markers (p-RIP1, p-RIP3 and p-MLKL). Scale bar: 10 μm. (D) Morphological analysis of liver tissues using H&E staining ($n = 5$). Dashed lines demarcate the necrotic regions. Scale bar: 50 μm. (E) The macroscopic observation to assess the liver injury ($n = 5$). (F) Representative images of TUNEL staining (green) in liver tissues at 12 h after the adjuvant induction ($n = 5$). Scale bar: 40 μm. (G, H) Liver function analysis by detecting ALT (G) and AST (H) in serum ($n = 5$). (I) Representative distribution and intensity of Cy5-R3-Dz in control or Con A mice after the intravenous injection of AP/Cy5-R3-Dz at different time points ($n = 3$). (J) Expression of RIP3 in liver tissues detected by immunochemistry ($n = 5$). Scale bar: 40 μm. Data are presented as mean ± SD, and one-sided statistical analysis is measured by one-way ANOVA with LSD test (G, H).

upregulated in affected tissues of RA patients as validated by published microarray data (GSE97779), indicating a crucial link between necroptosis and inflammation, key processes in the pathology of RA (Fig. 10A). Thus, a collagen-induced arthritis (CIA) model was established to evaluate the combined therapeutic efficacy of R3-Dz and MCC950 (Fig. 10B). In the inflamed joints of CIA mice, the levels of RIP1, RIP3 and NLRP3 notably increased, and synovial macrophages displayed higher levels of phosphorylated necrotic proteins. This phenomenon suggested that macrophages in the inflamed joints underwent programmed

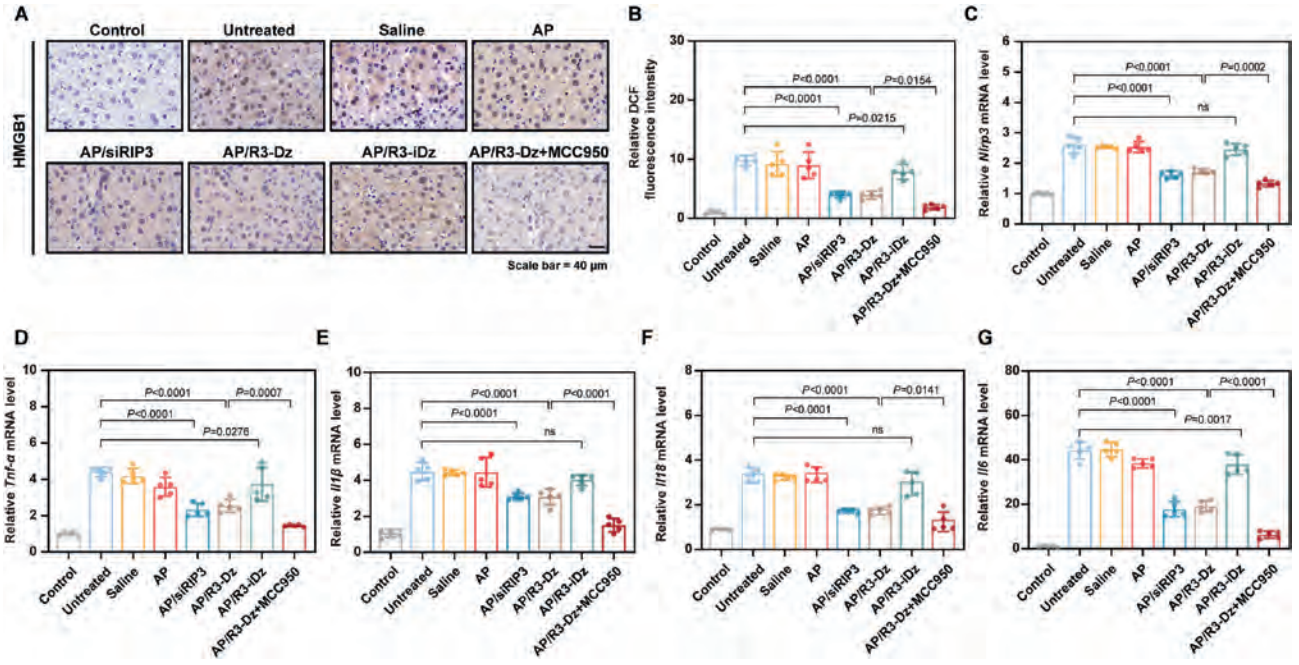

Figure 9 The combination R3-Dz and MCC950 protected against liver necrosis in experimental AIH. (A) Expression of HMGB1 in liver tissues detected by immunochemistry ($n = 5$). Scale bar: 40 μm. (B) The statistical quantification of fluorescence intensity of ROS in liver tissues of Con A mice with different treatments ($n = 5$). (C) *Nlrp3* mRNA level in liver tissues detected by qPCR ($n = 5$). (D−G) Relative *Tnf* (D), *Il1β* (E), *Il18* (F) and *Il6* (G) levels in the liver tissues of Con A mice measured by qPCR ($n = 5$). Data are presented as mean ± SD, and one-sided statistical analysis is measured by one-way ANOVA with LSD test (B−G).

necroptosis, potentially initiating the NLRP3-mediated inflammatory response (Fig. 10C and Supporting Information Figs. S45−S47). To quantify the severity of arthritis, the thickness change of paws was measured across various administration groups (Fig. 10D and E, Supporting Information Fig. S48). Compared to arthritic mice, treatments with saline, AP and AP/R3-iDz did not result in significant reduction in the thickness of paws. However, the mice treated with AP/siRIP3 and AP/R3-Dz nanoparticles showed partial remission in paw swelling, and the combination of AP/R3-Dz and MCC950 exhibited a marked reduction in swelling, nearly approaching the normal level. Clinical scoring for swelling and erythema also supported these findings, in which R3-Dz demonstrated significant improvements in clinical scores and the combination with MCC950 further enhanced these outcomes (Supporting Information Fig. S49). Bone erosion and remodeling, hallmarks of the late stage of RA, was evaluated using micro-computed tomography (micro-CT). In untreated, saline, AP and AP/R3-iDz groups, the inflamed ankle joints displayed surface roughness, significant bone erosion, and abnormal ossification (Fig. 10F and Supporting Information Fig. S50). Conversely, AP/R3-Dz and AP/siRIP3 nanoparticles resulted in an increased proportion of dense bone mass and moderately reduced bone erosion. Notably, the AP/R3-Dz and MCC950 group exhibited the highest bone integrity, closely reaching the normal level, as evidenced by enhanced bone formation parameters such as bone volume/tissue volume (*BV*/*TV*), bone surface/tissue volume (*BS*/*TV*) and an improved cortical and trabecular microstructure (Supporting Information Fig. S51). Consistent with the previously observed results, both AP/R3-Dz group and the AP/R3-Dz and MCC950 group facilitated the bone damage repair in arthritic joints. This improvement was evidenced by a significant increase in osteocalcin (OCN) expression, with the prominent enhancement in the AP/R3-Dz and MCC950 group (Supporting Information Fig. S52). These findings indicated that AP/R3-Dz offered substantial protection against bone damage and destruction in RA.

Further, the combination of AP/R3-Dz and MCC950 proved to be more effective in rescuing bone erosion, highlighting its superior therapeutic potential in the management of arthritic bone deterioration. Arthritis usually impairs ankle joint function, leading to physical disability. To evaluate the impact of different treatments on the mobility of arthritic mice, balance beam tests were conducted (Supporting Information Fig. S53). Arthritic mice experienced motor coordination deficits, as indicated by more frequent slips and longer time to cross the beam. In contrast, the mice treated with AP/R3-Dz and AP/siRIP3 nanoparticles demonstrated improved mobility with crossing the beam within 9.5 s, suggesting effective relief from joint ankylosis and walking disability. Notably, the combination treatment exhibited the most significant improvement with 60.7% reduction in time taken to cross the beam, indicating a stronger restoration of joint function. Moreover, the H&E staining of affected joints revealed significant inflammatory cell migration, bone erosion and narrowed joint space in mice treated with saline, AP and AP/R3-iDz (Fig. 10G). However, the reduced inflammatory infiltration and synovial hyperplasia have been observed in the mice treated with AP/R3-Dz and AP/siRIP3 nanoparticles, with the MCC950 intervention further deceasing the synovitis scores (Supporting Information Fig. S54). In addition, Safranin O/Fast Green and toluidine blue staining highlighted severe cartilage damage in arthritic mice, with evident chondrocyte loss and proteoglycan depletion, as reflected by elevated Mankin score (Fig. 10H and I, Supporting Information Fig. S55). In contrast, treatments with AP/R3-Dz and AP/siRIP3 nanoparticles resulted in a noticeable attenuation of

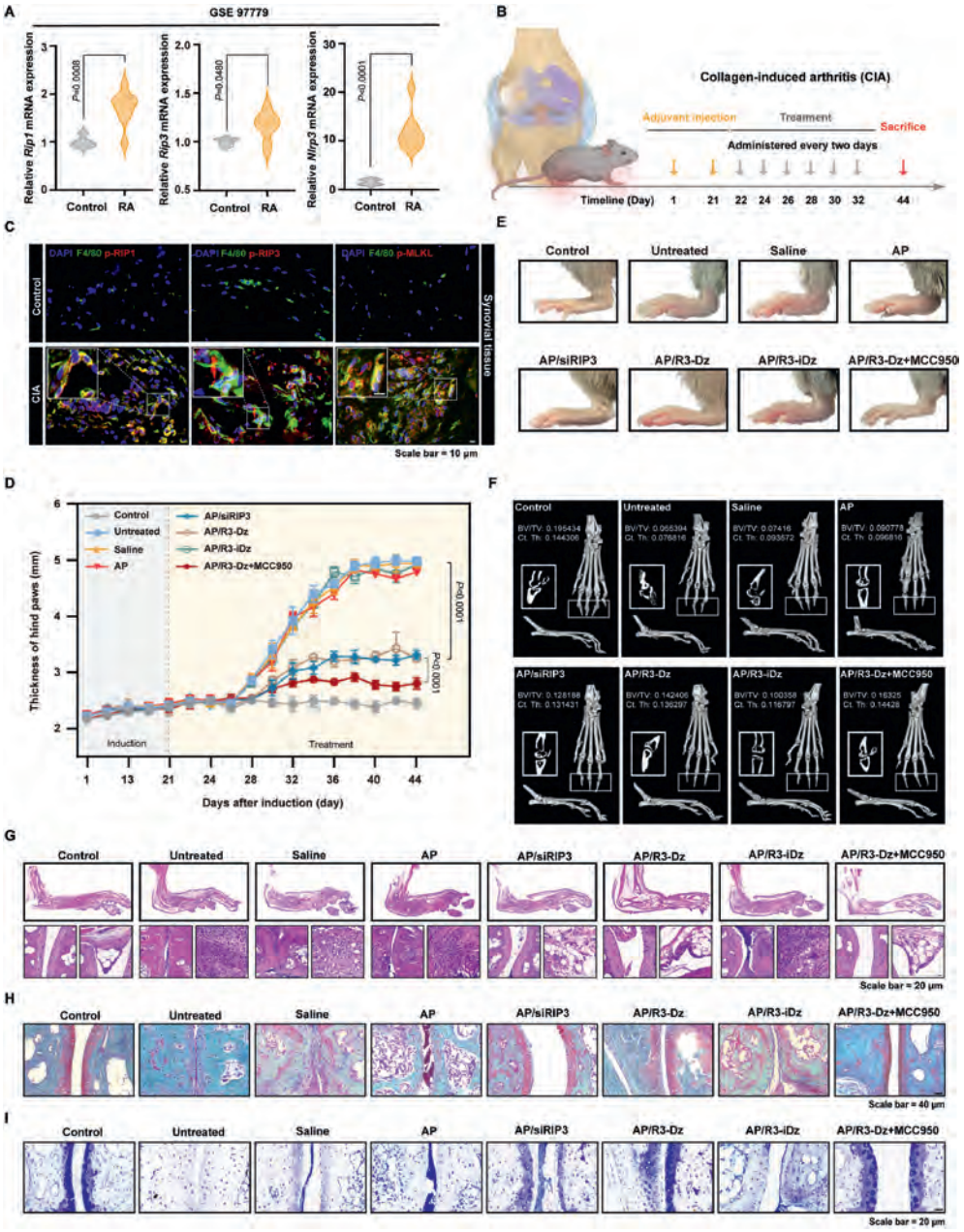

Figure 10 R3-Dz and MCC950 combination averted the articular damage in experimental RA. (A) The *Rip1*, *Rip3* and *Nlrp3* mRNA levels in the synovial macrophages from healthy individuals ($n = 5$) and RA patients ($n = 9$). Comparisons between two experimental groups are performed by two-tailed unpaired Student's *t*-test. (B) Schematic diagram of the CIA mice establishment and the treatment protocol. (C) Multiplex immunofluorescence staining of synovial tissues in normal and CIA mice employing macrophages (F4/80) and necrotic markers (p-RIP1, p-RIP3 and p-MLKL). Scale bar: 10 μm. (D) The thickness of hind paws during the period of 44 days post-adjuvant induction ($n = 5$). (E) The macroscopic observation to assess the severity of soft tissue swelling at Day 44 post-adjuvant induction ($n = 5$). (F) Representative micro-CT images of arthritis mice after different treatments at the Day 44 post-adjuvant induction ($n = 5$). (G) Histological changes of ankle joints analyzed by H&E staining. Region represents the infiltrate of synovial tissues and the bone erosion, respectively ($n = 5$). Scale bar: 20 μm. (H, I) Articular cartilages of ankle joints identified by Safranin O/Fast Green staining and toluidine blue staining. Scale bar: 40 μm and 20 μm, respectively ($n = 5$). Data are presented as mean ± SD, and one-sided statistical analysis is measured by one-way ANOVA with LSD test.

cartilage damage. Most significantly, the AP/R3-Dz and MCC950 group showed a marked reduction in Mankin scores, indicating substantial cartilage preservation by the combined treatment. These findings suggested that the AP/R3-Dz treatment effectively mitigated the inflammatory cell infiltration and the cartilage damage in RA, demonstrating its significant therapeutic efficacy. The addition of MCC950 to the AP/R3-Dz treatment amplified these benefits, leading to greater reduction in histopathological damage to cartilage. This result highlighted the enhanced potential of combination therapy in addressing the RA-associated joint pathology, exhibiting the treatment effect of AP/R3-Dz and MCC950.

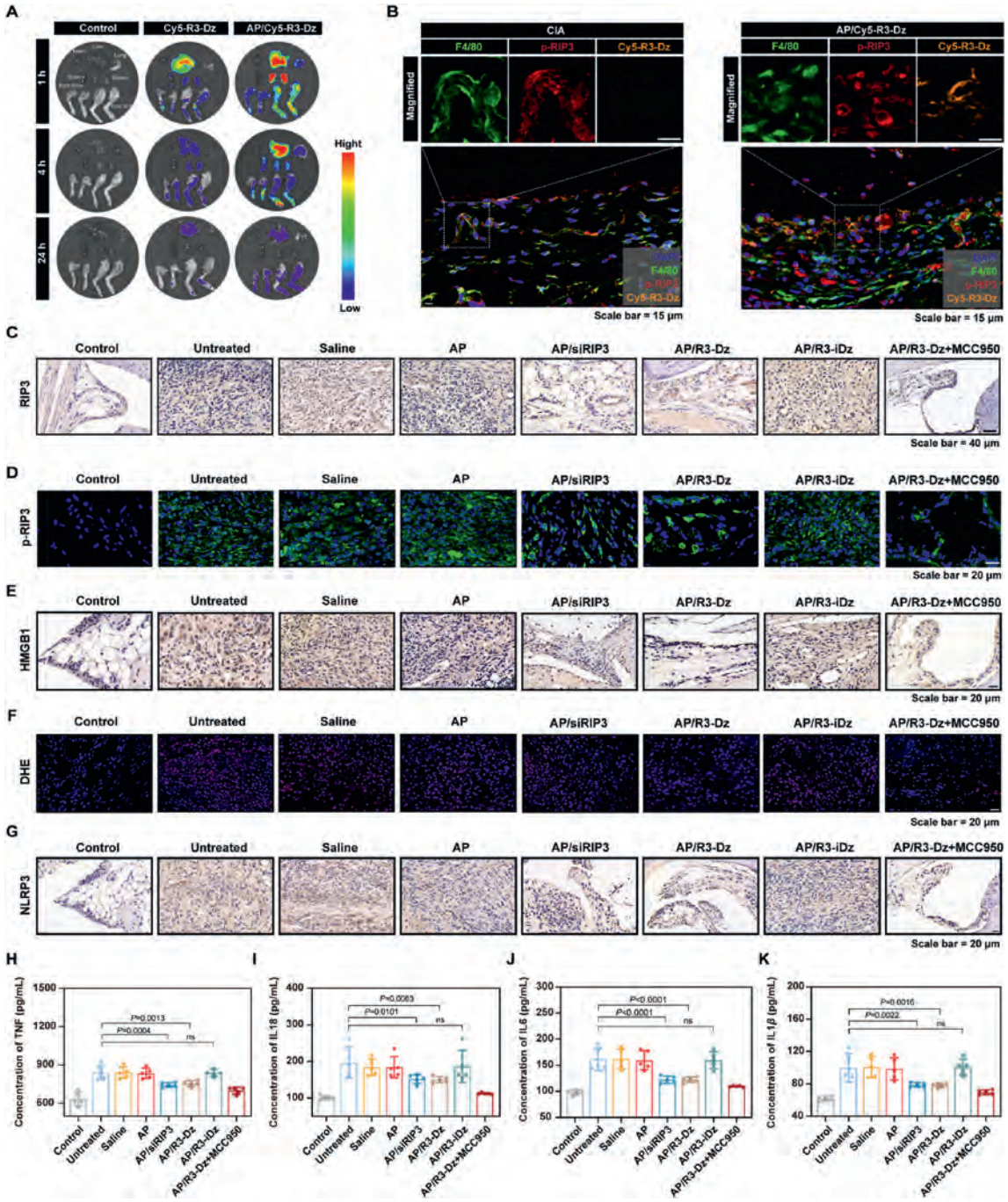

Figure 11 The R3-Dz and MCC950 combination attenuated the NLRP3-mediated necroinflammation in experimental RA. (A) *Ex vivo* biodistribution of free Cy5-R3-Dz and AP/Cy5-R3-Dz nanoparticles in CIA mice at 1, 4 and 24 h post-administration ($n = 3$). (B) Distribution of AP/Cy5-R3-Dz nanoparticles in the synovium of CIA mice using multiplex immunofluorescence. Nuclei, blue (DAPI); Cy5-R3-Dz, orange; F4/80, green; p-RIP3, red. Scale bar: 15 μm. (C) The RIP3 expression in arthritic joints detected by immunochemistry ($n = 5$). Scale bar: 40 μm. (D) Expression of p-RIP3 in arthritic joints detected by immunofluorescence ($n = 5$). Scale bar: 20 μm. (E) Expression of HMGB1 and NLRP3 in arthritic joints detected by immunochemistry ($n = 5$). Scale bar: 20 μm. (F) Expression of ROS in arthritic joints detected by immunofluorescence ($n = 5$). Scale bar: 20 μm. (G) Expression of NLRP3 in arthritic joints detected by immunochemistry ($n = 5$). (H–K) The levels of TNF (H), IL18 (I), IL6 (J) and IL1β (K) detected by ELISA method at Day 44 post-adjuvant induction ($n = 5$). Data are presented as mean ± SD, and one-sided statistical analysis is measured by one-way ANOVA with LSD test.

After evaluating the efficacy of R3-Dz in protecting against the bone damage in experimental RA, we next focused on understanding the biodistribution of AP/R3-Dz nanoparticles. This shift from therapeutic outcome to pharmacokinetic profiling is crucial to understand how these nanoparticles navigate the body and specifically target the inflamed joints, a key factor in their

therapeutic efficacy. After systemic administration, both free Cy5-R3-Dz and AP/Cy5-R3-Dz were predominantly accumulated in liver and kidneys, and metabolized within 24 h (Fig. 11A and Supporting Information Fig. S56). Nevertheless, AP/Cy5-R3-Dz exhibited enhanced fluorescence in inflamed joints compared to free Cy5-Dz, indicating preferential targeting and prolonged retention in these areas due to the ELVIS effect. Further, immunofluorescence analysis confirmed the presence of AP/R3-Dz nanoparticles in the necroptotic macrophages of synovium (Fig. 11B and Supporting Information Fig. S57). This targeted effect indicated that the AP/R3-Dz nanoparticles were efficiently homing in on the key sites of inflammation and tissue damage in experimental RA, potentially enhancing the therapeutic efficacy by directly modulating the cells related to the pathology. Moreover, we analyzed how this localized accumulation influenced the necroptosis and inflammatory response in experimental RA, demonstrating the anti-necrotic effect of AP/R3-Dz nanoparticles with the significantly decreased levels of RIP3, p-RIP3, HMGB1 and ROS in the synovium of inflamed joints by targeting necrotic macrophages (Fig. 11C−F and Supporting Information Figs. S58−S62). This effect was further enhanced in the AP/R3-Dz and MCC950 group, suggesting that MCC950 attenuated the necroptosis possibly by inhibiting the activation of NLRP3 inflammasome. Moreover, the assessment of NLRP3 and downstream pro-inflammatory cytokines such as TNF, IL6, IL1β and IL18 revealed their significant elevation in arthritic mice (Fig. 11G−K, Supporting Information Figs. S63 and S64). While AP/R3-Dz and AP/siRIP3 treatments effectively reduced the expression of NLRP3 and related cytokines, the combination of AP/R3-Dz with MCC950 exhibited a more profound inhibition, markedly lowering these cytokines to normal levels. These findings collectively highlighted the strong therapeutic efficacy of AP/R3-Dz in mitigating both necroptosis and NLRP3-mediated inflammation in RA, with the combination of AP/R3-Dz and MCC950 showing enhanced therapeutic effect. In addition, no observable damage to major organs was found and no significant differences in blood biochemistry were detected, both implying the biocompatibility of AP/R3-Dz nanoparticles and MCC950 (Supporting Information Figs. S65 and S66). Finally, the pharmacokinetics of AP/Cy5-R3-Dz nanoparticles were evaluated in healthy rats after the intravenous injection (Supporting Information Fig. S67). The AP/R3-Dz nanoparticles showed a significantly longer half-life ($t_{1/2}$) than free Cy5-R3-Dz, with $t_{1/2}$ of AP/R3-Dz nanoparticles ($\approx$6.33 h) almost 6-fold higher than that of free Cy5-R3-Dz ($\approx$1.32 h), demonstrating that the AP carrier could prolong the blood circulation of Cy5-R3-Dz and protect it from the degradation by serum nuclease. In comparison to Cy5-R3-Dz, the significantly enhanced area under the curve (AUC) and mean residence time (MRT) of AP/R3-Dz nanoparticles demonstrated the remarkable protective efficacy of AP dendrimer against the nuclease-mediated R3-Dz degradation in the blood, thereby enhancing the ELVIS effect and delaying the elimination by mononuclear phagocyte system.

4. Discussion

Acute inflammation is fundamentally an innate defense mechanism, aimed to respond to and resolve harmful stimuli. However, when the innate immune response is insufficient to mitigate excessive inflammatory processes, it results in persistent tissue damage. This process often culminates in chronic inflammation, which significantly contributes to the disruption of tissue homeostasis. The current therapeutic strategy, predominantly focusing on the inhibition of cytokines, has shown limitations in effectively treating such inflammatory diseases. This situation motivates the need for a more comprehensive understanding of the underlying mechanism. Necroptosis, a caspase-independent cell death program, causes the disruption of plasma membrane and the release of intracellular DAMPs. This process plays a pivotal role in contributing to the recruitment of immune cells and the induction of inflammation. Concurrently, the excessive presence of pro-inflammatory cytokines in the milieu induces the cell death, thereby perpetuating a deleterious cycle to intensify the inflammatory process. This intricate interplay between necroptosis and inflammation contributes significantly to the pathophysiology of chronic inflammatory diseases, highlighting the need for targeted therapeutic interventions addressing these interconnected mechanism. In the context of necroptosis, RIP1 and RIP3 emerge as pivotal components within the necrosome, playing a central role in orchestrating programmed cell death. Specifically, we aimed to investigate the potential of rescuing cell death and mitigating the inflammatory response through precise intervention targeting RIP1 and RIP3. Our results demonstrated that the inhibition of RIP3 was more effective in improving the cell death compared to RIP1. Besides as a crucial component of necrosome, RIP1 serves as the molecular scaffold to recruit downstream molecules and stabilize TNFR1−FADD−RIP1 complex I, eventually facilitating the transmission of pro-survival signals[11]. ZBP1 has been reported to be an alternative effector to induce the RIP3-dependent necroptosis in the absence or mutation of RIP1[36]. RIP3 forms functional amyloid signaling complexes in a cell-autonomous manner, independent on RIP1[37]. The *Rip1*$^{-/-}$ mice showed severe inflammation and high level of apoptosis in multiple tissues, ultimately leading to systemic cell death and perinatal lethality[38]. However, the loss of either RIP3 or MLKL contributed to the partial amelioration of survive and inflammatory phenotype observed in newborn *Rip1*$^{-/-}$ mice[39]. Our observation also highlighted that the inhibition of RIP3 not only served to prevent the necroptotic process but also exerted a suppressive effect on the cytokine production. This dual functionality of RIP3 inhibition suggested that RIP3 as a pivotal target for intervention could be used to modulate both cell death pathways and inflammatory responses.

To guide the design and screening of DNAzymes, conserved structural domains of substrate RNA and their predicted kinetic parameters were systematically analyzed. Among the RIP3 DNAzyme libraries, R3-Dz stood out for its exceptional efficiency in silencing intracellular RIP3 expression in RAW264.7 cells, highlighting its potential as a therapeutic agent. Although both R3-Dz and siRNA achieved effective gene silencing of *RIP3*, R3-Dz showed significant advantages over siRNA with regards to catalytic activity, structural stability and substrate specificity. siRNA is typically consumed after the mRNA degradation by RNA-induced silencing complex (RISC), precluding its potential for multiple rounds of reuse[40]. In contrast, R3-Dz demonstrates multiple-turnover catalytic activity to cleave the multiple RNA substrates, facilitating sustained and potentially more efficient gene silencing. Further, R3-Dz, a synthetic single-stranded DNA molecule capable of catalyzing chemical reactions, exhibits high structural stability and great resistance to the nuclease degradation in physiological environment in comparison to siRNA. Moreover, the 10-23 DNAzyme-mediated RNA cleavage has been elucidated to enable the precise targeting of specific nucleotide mutations

responsible for the disease-associated phenotypes[41], indicating that R3-Dz possessed excellent specificity for cleaving the target RNA substrates.

MD simulation has elucidated the cleavage mechanism of R3-Dz, revealing a decrease in free energy following cleavage. This finding suggested that R3-Dz possessed the propensity to spontaneously cleave *RIP3* mRNA. Importantly, dG_{14} of 10-23 DNAzyme has been identified to interact with the O2′ of rG_0 more frequently than hydrated Mg^{2+}, suggesting its essential role as a Brønsted base in deprotonating O2′[28]. In line with these findings, our results demonstrated that the complexes containing dG_{14} mutation displayed lower stability and altered the interaction between catalytic loop and cleavage site, highlighting the importance of dG_{14} in preparing catalytic configuration for the deprotonation of O2′ atom on the rA_0 residue. This specific spatial arrangement between the O2′ of rA_0 and the O5′ of rU_{-1} optimally positioned the system for the imminent nucleophilic attack by the O2′ oxyanion on the adjacent phosphodiester bond. Consequently, these findings offered profound insights into the structure and function of R3-Dz complex, revealing the precise molecular interaction orchestrated by R3-Dz for targeted RNA cleavage and emphasizing its efficiency and specificity in catalysis. The introduction of a chemical modification such as OMe substitution at the dG_{14} position in the scaffold could favor the formation of a catalytically active conformation by altering the equilibrium of 10−23 topology, thereby enhancing the catalytic activity[41]. Accordingly, we modified dG_{14} in R3-Dz with an OMe group to enhance its biological functionality, aiming at improved performance within the intracellular environment.

To enhance the stability and transfection of R3-Dz, PAMAM dendrimer was modified with nucleobase analog 2-amino-6-chloropurine to construct a PAMAM derivative (namely AP). The AP carrier exhibited notable efficiency in the compaction of nucleic acids, including exceptional capability in both the assembly and stabilization of R3-Dz against the degradation of serum nucleases. Although strong positive charge density of dendrimer was beneficial for forming stable nanoparticles with nucleic acids, it could meanwhile make the release of nucleic acids in the cytosol more challenging. The incorporation of 2-amino-6-chloropurine, a purine derivative, compensated for the reduced charge-induced affinity loss by forming hydrogen bonds with nucleic acids, which ensured stable complex formation and facilitated a more controlled and efficient release in the cells. The AP/R3-Dz nanoparticles exhibit acid-sensitive release properties due to the breaking of hydrogen bond and the structural transformation at low pH, promoting on-demand drug release in the acidic inflammatory microenvironment[42]. Moreover, high positive charge of PAMAM was associated with the cytotoxicity, as it led to non-specific interaction with negatively charged cellular membrane and components. Reducing the positive charge after the modification could mitigate this issue, enhancing the derivative's biocompatibility. These properties collectively endowed the carrier AP with superior transfection efficiency of R3-Dz compared to its unmodified counterpart.

Macrophages, central to the immune system, play a key role in necroptosis due to their ability to detect pathogens, modulate inflammatory responses, and directly engage in necroptosis such as TNFR1 and TLR4 signaling pathways[30]. Since their significance in various diseases and major role in cytokine production, macrophages are indispensable for understanding the intersection of cell death, inflammation, and disease progression. Thus, it is essential to investigate the specific effects of R3-Dz on macrophage-mediated necroptotic pathways and inflammatory responses, which could enhance the comprehension of its potential therapeutic application. LPS and Z-VAD induced the necroptosis in macrophages by triggering TLR4 signaling pathway and inhibiting caspase-8, respectively, leading to the activation of RIP1−RIP3−MLKL pathway[11]. Particularly, the presence of elevated level of RIP3 serves as a critical determinant in predicting the susceptibility to necroptotic death induced by specific stimuli[43]. The introduction of R3-Dz effectively targeted and inhibited RIP3 expression in macrophages, showing a significant anti-necroptotic effect which was evidenced by the suppression of organelle swelling, preservation of cell membrane integrity, and improved cell viability. Further, the transfection of R3-Dz led to the significant suppression of RIP1 and RIP3 interaction, the reduction in phosphorylated RIP1 and MLKL levels and the attenuation of necroptotic pathways. By inhibiting the formation of necrosome, R3-Dz disrupted a critical step in the necroptotic signaling cascade, highlighting its specific targeting of RIP3 and its pivotal role in the modulation of necroptosis. RIP3 is known to activate the NLRP3 inflammasome through multiple mechanisms, including the induction of necrosome formation that facilitates the membrane translocation of MLKL[44]. This translocation results in a decreased concentration of intracellular potassium ions, triggering the assembly of NLRP3 inflammasome. Meanwhile, the release of HMGB1 and ROS from necrotic macrophages acts as priming and activating signals for NLRP3 inflammasome, thereby driving the inflammatory response[12]. The HMGB1 expression has been reported to be closely associated with RIP3 in the necrotic process[45,46]. The *RIP3* knockout mice showed a reduction in sepsis and donor kidney inflammatory damage, which was found to be related to a decrease in HMGB1 release[45]. Meanwhile, the RIP3 inhibitor could reduce the HMGB1 level and protect the animals from the jejunal morphological injury[46]. Further, HMGB1 acts in an autocrine and/or paracrine manner to stimulate the production of pro-inflammatory cytokines *via* TLR4/Interleukin-1 receptor associated kinase-4 (IRAK4)-dependent mechanism. The HMGB1 also acts as the priming effector for NLRP3 inflammasome activation, which results in robust expression of the inflammasome components. Following ROS activation, NLRP3 oligomerizes and recruits the apoptosis-associated speck-like (ASC) adapter and pro-caspase-1, leading to the cleavage of pro-IL-1β and pro-IL-18 into their mature forms. Moreover, RIP3 can promote the NLRP3 inflammasome and IL1β inflammatory responses, independence on MLKL and necroptotic cell death[47]. The role of RIP3 in mediating the NLRP3 inflammasome-driven inflammation was further corroborated by the findings that the knockdown of RIP3 reduced the expression of HMGB1, ROS and pro-inflammatory cytokines. Moreover, the inflammatory responses, in turn, exacerbates the necrosis program through the activation of ROS release, stimulating RIP1 autophosphorylation and RIP3 phosphorylation[14]. This forms a complex loop that further amplifies the RIP3−NLRP3-mediated necroinflammation. As expected, AP/R3-Dz nanoparticles significantly inhibited the HMGB1 release and ROS production, effectively suppressing the NLRP3-mediated inflammatory pathway and mitigating the necroinflammatory process. This behavior positioned AP/R3-Dz as a promising therapeutic agent with the potential to ameliorate the necroptosis-induced inflammatory diseases and autoimmune syndromes. Consequently, AP/R3-Dz nanoparticles were further investigated for its anti-inflammatory and tissue repair properties in various types of arthritis to evaluate their therapeutic potential in targeting RIP3-mediated necroptosis and inflammation.

GA, characterized by acute inflammatory response to uric acid crystals deposited in joints, serves as an ideal model to evaluate the effects of R3-Dz due to its pathological relevance to necroptosis. This relevance includes the activation of specific cell death pathways, including the upregulation of RIP1, RIP3 and NLRP3, alongside the accumulation of necrotic synovial macrophages, offering precise biomarkers to assess the therapeutic impact of intervention. Further, GA exemplifies the phenomenon of necroinflammation, providing a platform to explore not only the anti-necroptotic effects of R3-Dz but also its potential to mitigate inflammation. The use of intra-articular injection in this model also allowed for detailed insights into the direct effects of R3-Dz on inflamed tissues. The AP/R3-Dz nanoparticles demonstrated significant therapeutic efficacy in GA model, evidenced by their ability to modulate key pathological processes. Upon intra-articular administration, these nanoparticles effectively reduced the joint swelling, curtailed the infiltration of synovial inflammatory cells, and decreased the secretion of pro-inflammatory cytokines. This reduction in inflammatory phenomenon was paralleled by a notable decrease in the expression levels of RIP3, HMGB1, ROS and NLRP3 in the joint, indicating a targeted suppression of the RIP3−NLRP3-mediated necroinflammatory pathway. Such findings not only validated the direct therapeutic effects of R3-Dz on inflamed tissues but also highlighted the potential of intra-articular delivery as a strategy for localized intervention in necroptosis-associated inflammatory conditions. The observed outcome suggested that AP/R3-Dz nanoparticles held promise to address the underlying mechanism of necroinflammation in GA, paving the way for novel therapeutic approaches in the management of this disorder and other chronic inflammatory diseases. Inspired by the promising advantages in GA, we next extended our investigation to evaluate the effect of R3-Dz nanoparticles in AIH model, targeting systemic inflammation and autoimmunity. AIH represents a distinct pathological entity from GA, characterized by a pervasive inflammatory response leading to liver damage and potential failure. Intravenous delivery of AP/R3-Dz nanoparticles significantly mitigated hepatic injury, ameliorated liver dysfunction, decreased mortality rate, and suppressed inflammatory responses through targeted inhibition of cellular necrosis. Unlike GA, where local inflammation predominates, AIH involves an acute systemic inflammatory response, necessitating a more comprehensive therapeutic strategy. MCC950, a specific inhibitor of NLRP3 inflammasome, complemented the R3-Dz's inhibition of necroptosis by simultaneously targeting the inflammatory cascade that contributes to the AIH' severity. Following the intravenous administration of AP/R3-Dz nanoparticles, they were passively accumulated in the inflamed liver, which was facilitated by the ELVIS effect. The subsequent intraperitoneal injection of MCC950 enhanced the suppression of acute hepatic injury, effectively augmenting the therapeutic impact on disease progression by improving the anti-inflammatory and protective effects initiated by R3-Dz. Critically, no significant renal or liver damages were detected in the treatment cohorts, indicating the favorable biocompatibility of the combined AP/R3-Dz and MCC950 therapy. R3-Dz and MCC950 function like a precise "clamp", each targeting a distinct aspect of necroinflammation: R3-Dz inhibited the necroptosis, halting the cellular death cascade, while MCC950 suppressed the NLRP3 inflammasome, curbing the inflammatory response. Together, they formed a comprehensive blockade against the dual threats of cell death and inflammation, effectively "clamping" the necroinflammatory cycle and achieving significant anti-inflammatory and tissue repair outcomes.

RA is a chronic autoimmune disease characterized by systemic inflammation and progressive joint destruction, where the dysregulation of cell death processes including apoptosis and necroptosis, plays a pivotal role in both its initiation and advancement. The involvement of RIP3−NLRP3 in mediating necroinflammation within RA, highlighted by the elevated level of these factors in synovial tissues, suggested the potential therapeutic targets for intervention. Upon the intravenous administration, AP could prolong the circulation time of R3-Dz, endowing it with long-circulating properties that facilitate the preferential uptake of R3-Dz by necrotic macrophages in the hyperplastic synovial tissues. The intracellular presence of R3-Dz led to a notable reduction in RIP3 expression, thereby mitigating the RIP3−NLRP3-driven necroinflammatory process. This action resulted in decreased level of inflammatory cytokines, thereby reducing immune cell recruitment, synovial macrophage infiltration, and the inflammatory activation of synovial fibroblasts and chondrocytes. Further, it could suppress the release of matrix metalloproteinases, ameliorating cartilage and bone damage and thus restoring joint mobility in CIA mice. To enhance this therapeutic strategy, MCC950 acted to further inhibit the activation of NLRP3 inflammasome, contributing to a more pronounced suppression of necrosis progression and tissue damage. The dual intervention through the combination of AP/R3-Dz nanoparticles and MCC50 effectively blocked the RIP3−NLRP3-mediated necroinflammatory loop, offering significant protection against RA.

5. Conclusions

In summary, our investigations demonstrated the potent efficacy of R3-Dz in inhibiting the necroptosis, offering a promising therapeutic approach for inflammatory diseases. Through targeted dual inhibition of NLRP3-mediated necroinflammation, AP/R3-Dz nanoparticles and MCC950 significantly reduced the inflammatory markers and mitigated the disease symptoms in all tested models, indicating their broad therapeutic potential. These findings also reinforced the role of necroptosis in the pathology of arthritis and positioned R3-Dz as a valuable candidate for further development and clinical exploration.

Acknowledgments

The work was supported by the National Natural Science Foundation of China (32471315, 32000897, U24A20365 and 32271319), the Science and Technology Department of Jilin Province (YDZJ202301ZYTS537, China), the Development and Reform Commission of Jilin Province (2023C015 and 2024C013-8, China), the Fundamental Research Funds of the Central Universities, China (2024-JCXK-11) and the Innovation Program for Graduate Students of Jilin University (101832020CX095, China).

Author contributions

Jiaxin Jia: conceptualization, investigation, methodology, funding acquisition, validation, data curation, writing-original draft. Hugang Zhang: investigation, visualization, validation, formal analysis, resources. Guangxu Fang: formal analysis, validation,

writing-original draft. Yang Li: investigation, methodology, validation, data curation. Kai Wen: investigation, validation. Hanyu Liu: investigation, data Curation. Haobo Han: conceptualization, funding acquisition, supervision, project administration, writing-review&editing. Quanshun Li: conceptualization, funding acquisition, supervision, project administration, writing-review&editing.

Conflicts of interest

The authors declare no conflicts of interest.

Appendix A. Supporting information

Supporting information to this article can be found online at https://doi.org/10.1016/j.apsb.2025.09.002.

References

1. Medzhitov R. The spectrum of inflammatory responses. *Science* 2021; **374**:1070−5.
2. Crum RJ, Huckestien BR, Dwyer G, Mathews L, Nascari DG, Hussey GS, et al. Mitigation of influenza-mediated inflammation by immunomodulatory matrix-bound nanovesicles. *Sci Adv* 2023;**9**: eadf9016.
3. Huang Q, Doyle R, Chen S, Sheng Q, Misharin AV, Mao Q, et al. Critical role of synovial tissue-resident macrophage niche in joint homeostasis and suppression of chronic inflammation. *Sci Adv* 2023;**7**: eabd0515.
4. Manolakou T, Nikolopoulos D, Gkikas D, Filia A, Samiotaki M, Stamatakis G, et al. ATR-mediated DNA damage responses underlie aberrant B cell activity in systemic lupus erythematosus. *Sci Adv* 2022; **8**:eabo5840.
5. Javaid N, Patra MC, Cho DE, Batool M, Kim Y, Choi GM, et al. An orally active, small-molecule TNF inhibitor that disrupts the homotrimerization interface improves inflammatory arthritis in mice. *Sci Signal* 2022;**15**:eabi8713.
6. Peredo AP, Gullbrand SE, Friday CS, Orozco BS, Dehghani B, Jenk AC, et al. Tension-activated nanofiber patches delivering an anti-inflammatory drug improve repair in a goat intervertebral disc herniation model. *Sci Transl Med* 2023;**15**:eadf1690.
7. Broderick L, Hoffman HM. IL-1 and autoinflammatory disease: biology, pathogenesis and therapeutic targeting. *Nat Rev Rheumatol* 2022;**18**:448−63.
8. Feist E, Mitrovic S, Fautrel B. Mechanisms, biomarkers and targets for adult-onset still's disease. *Nat Rev Rheumatol* 2018;**14**:603−18.
9. Gaujoux R, Starosvetsky E, Maimon N, Vallania F, Bar-Yoseph H, Pressman S, et al. Cell-centred meta-analysis reveals baseline predictors of anti-TNFα non-response in biopsy and blood of patients with IBD. *Gut* 2019;**68**:604−14.
10. Wallach D, Kang TB, Dillon CP, Green DR. Programmed necrosis in inflammation: toward identification of the effector molecules. *Science* 2016;**352**:aaf2154.
11. Zhu J, Xin M, Xu C, He Y, Zhang W, Wang Z, et al. Ligand-based substituent-anchoring design of selective receptor-interacting protein kinase 1 necroptosis inhibitors for ulcerative colitis therapy. *Acta Pharm Sin B* 2021;**11**:3193−205.
12. Kwon HK, Lee I, Yu KE, Cahill SV, Alder KD, Lee S, et al. Dual therapeutic targeting of intra-articular inflammation and intracellular bacteria enhances chondroprotection in septic arthritis. *Sci Adv* 2021; **7**:eabf2665.
13. Zhang C, Wang H, Yang XH, Fu Z, Ji XR, Shi YF, et al. Oral zero-valent-molybdenum nanodots for inflammatory bowel disease therapy. *Sci Adv* 2022;**8**:eabp9882.
14. Zhang YY, Su SS, Zhao SB, Yang ZT, Zhong CQ, Chen X, et al. RIP1 autophosphorylation is promoted by mitochondrial ROS and is essential for RIP3 recruitment into necrosome. *Nat Commun* 2017;**8**: 14329.
15. Linkermann A. Death and fire-the concept of necroinflammation. *Cell Death Differ* 2019;**26**:1−3.
16. Yan JQ, Ran MX, Shen X, Zhang HB. Therapeutic DNAzymes: from structure design to clinical applications. *Adv Mater* 2023;**35**: e2300374.
17. Wang R, He WH, Yi X, Wu ZK, Chu X, Jiang J. Site-specific bioorthogonal activation of DNAzymes for on-demand gene therapy. *J Am Chem Soc* 2023;**145**:17926−35.
18. Cho EA, Moloney FJ, Cai H, Au Yeung A, China C, Scolyer RA, et al. Safety and tolerability of an intratumorally injected DNAzyme, Dz13, in patients with nodular basal-cell carcinoma: a phase 1 first-in-human trial (DISCOVER). *Lancet* 2013;**381**:1835−43.
19. Krug N, Hohlfeld JM, Kirsten AM, Kornmann O, Beeh KM, Kappeler D, et al. Allergen-induced asthmatic responses modified by a GATA3-specific DNAzyme. *N Engl J Med* 2015;**372**:1987−95.
20. Silverman SK. Catalytic DNA: scope, applications, and biochemistry of deoxyribozymes. *Trends Biochem Sci* 2016;**41**:595−609.
21. Guo Y, Wu ZQ, Shen SL, Guo RM, Wang J, Wang WW, et al. Nanomedicines reveal how PBOV1 promotes hepatocellular carcinoma for effective gene therapy. *Nat Commun* 2018;**9**:3430.
22. Han HB, Xing JK, Chen WQ, Jia JX, Li QS. Fluorinated polyamidoamine dendrimer-mediated miR-23b delivery for the treatment of experimental rheumatoid arthritis in rats. *Nat Commun* 2023;**14**: 944.
23. Jiang K, Chen JY, Tai LY, Liu C, Chen XS, Wei G, et al. Inhibition of post-trabeculectomy fibrosis *via* topically instilled antisense oligonucleotide complexes co-loaded with fluorouracil. *Acta Pharm Sin B* 2020;**10**:1754−68.
24. Gusdon AM, Faraday N, Aita JS, Kumar S, Mehta I, Choi HA, et al. Dendrimer nanotherapy for severe COVID-19 attenuates inflammation and neurological injury markers and improves outcomes in a phase2a clinical trial. *Sci Transl Med* 2022;**14**:eabo2652.
25. Han HB, Yang JB, Wang YD, Chen WQ, Chen JW, Yang Y, et al. Nucleobase-modified polyamidoamine-mediated miR-23b delivery to inhibit the proliferation and migration of lung cancer. *Biomater Sci* 2017;**5**:2268−75.
26. Wei SM, Shao XX, Liu Y, Xiong BY, Cui PF, Liu ZL, et al. Genome editing of PD-L1 mediated by nucleobase-modified polyamidoamine for cancer immunotherapy. *J Mater Chem B* 2022;**10**: 1291−300.
27. Chen JX, Zhu HF, Xia JC, Zhu YT, Xia C, Hu ZH, et al. High-performance multi-dynamic bond cross-linked hydrogel with spatiotemporal siRNA delivery for gene−cell combination therapy of intervertebral disc degeneration. *Adv Sci* 2023;**10**:e2206306.
28. Borggräfe J, Victor J, Rosenbach H, Viegas A, Gertzen CGW, Wuebben C, et al. Time-resolved structural analysis of an RNA-cleaving DNA catalyst. *Nature* 2022;**601**:144−9.
29. Meng YS, Wang LF, Zhao GM, Diao JB, Qi ZB, Yu MY, et al. Hydrogel nanoparticles enable nucleation barrier regulation and ion anchoring as an alternative pathway for monosodium urate monohydrate crystallization control. *ACS Nano* 2024;**18**:13794−807.
30. He SD, Liang YQ, Shao F, Wang XD. Toll-like receptors activate programmed necrosis in macrophages through a receptor-interacting kinase-3-mediated pathway. *Proc Natl Acad Sci U S A* 2011;**108**: 20054−9.
31. Scaffidi P, Misteli T, Bianchi ME. Release of chromatin protein HMGB1 by necrotic cells triggers inflammation. *Nature* 2002;**418**: 191−5.
32. Mittal M, Siddiqui MR, Tran K, Reddy SP, Malik AB. Reactive oxygen species in inflammation and tissue injury. *Antioxidants Redox Signal* 2014;**20**:1126−67.
33. Mulay SR, Desai J, Kumar SV, Eberhard JN, Thomasova D, Romoli S, et al. Cytotoxicity of crystals involves RIPK3−MLKL-mediated necroptosis. *Nat Commun* 2016;**7**:10274.

34. Deutsch M, Graffeo CS, Rokosh R, Pansari M, Ochi A, Levie EM, et al. Divergent effects of RIP1 or RIP3 blockade in murine models of acute liver injury. *Cell Death Dis* 2015;**6**:e1759.
35. Anderton H, Wicks IP, Silke J. Cell death in chronic inflammation: breaking the cycle to treat rheumatic disease. *Nat Rev Rheumatol* 2020;**16**:496−513.
36. Kuriakose T, Man SM, Malireddi RK, Karki R, Kesavardhana S, Place DE, et al. ZBP1/DAI is an innate sensor of influenza virus triggering the NLRP3 inflammasome and programmed cell death pathways. *Sci Immunol* 2016;**1**:aag2045.
37. Zhang DW, Shao J, Lin J, Zhang N, Lu BJ, Lin SC, et al. RIP3, an energy metabolism regulator that switches TNF-induced cell death from apoptosis to necrosis. *Science* 2009;**325**:332−6.
38. Li XY, Zhang MM, Huang XY, Liang W, Li GQ, Lu XJ, et al. Ubiquitination of RIPK1 regulates its activation mediated by TNFR1 and TLRs signaling in distinct manners. *Nat Commun* 2020;**11**:6364.
39. Newton K, Dugger DL, Maltzman A, Greve JM, Hedehus M, Martin-McNulty B, et al. RIPK3 deficiency or catalytically inactive RIPK1 provides greater benefit than MLKL deficiency in mouse models of inflammation and tissue injury. *Cell Death Differ* 2016;**23**: 1565−76.
40. Dong Y, Siegwart DJ, Anderson DG. Strategies, design, and chemistry in siRNA delivery systems. *Adv Drug Deliv Rev* 2019;**144**:133−47.
41. Nguyen K, Malik TN, Chaput JC. Chemical evolution of an autonomous DNAzyme with allele-specific gene silencing activity. *Nat Commun* 2023;**14**:2413.
42. Liu Y, Bryantsev VS, Diallo MS, Goddard 3rd WA. PAMAM dendrimers undergo pH responsive conformational changes without swelling. *J Am Chem Soc* 2009;**131**:2798−9.
43. He SD, Wang L, Miao L, Wang T, Du FH, Zhao LP, et al. Receptor interacting protein kinase-3 determines cellular necrotic response to TNF-alpha. *Cell* 2009;**137**:1100−11.
44. Conos SA, Chen KW, De Nardo D, Hara H, Whitehead L, Núñez G, et al. Active MLKL triggers the NLRP3 inflammasome in a cell-intrinsic manner. *Proc Natl Acad Sci U S A* 2017;**114**:E961−9.
45. Murakami Y, Matsumoto H, Roh M, Giani A, Kataoka K, Morizane Y, et al. Programmed necrosis, not apoptosis, is a key mediator of cell loss and DAMP-mediated inflammation in dsRNA-induced retinal degeneration. *Cell Death Differ* 2014;**21**:270−7.
46. Liu YL, Xu Q, Wang Y, Liang TZ, Li XG, Wang D, et al. Necroptosis is active and contributes to intestinal injury in a piglet model with lipopolysaccharide challenge. *Cell Death Dis* 2021;**12**:62.
47. Wang XQ, Jiang W, Yan YQ, Gong T, Han JH, Tian ZG, et al. RNA viruses promote activation of the NLRP3 inflammasome through a RIP1−RIP3−DRP1 signaling pathway. *Nat Immunol* 2014;**15**: 1126−33.